Journal of Hydrology 556 (2018) 645–659

Contents lists available at ScienceDirect

Journal of Hydrology

journal homepage: www.elsevier.com/locate/jhydrol

Research papers

Evapotranspiration sensitivity to air temperature across a snow-influenced watershed: Space-for-time substitution versus integrated watershed modeling

S.M. Jepsen [a,b,*], T.C. Harmon [b], D.L. Ficklin [c], N.P. Molotch [d,e], B. Guan [e,f]

[a] University of Nevada, Global Water Center, 1664 N. Virginia St, Reno, NV 89557, USA
[b] University of California, School of Engineering, 5200 N. Lake Road, Merced, CA 95343, USA
[c] Indiana University, Department of Geography, 701 E. Kirkwood Avenue, Bloomington, IN 47405, USA
[d] University of Colorado, Geography Department and Institute of Arctic and Alpine Research, Guggenheim 110, 260 UCB, Boulder, CO 80309, USA
[e] California Institute of Technology, Jet Propulsion Laboratory, 4800 Oak Grove Drive, Pasadena, CA 91109, USA
[f] University of California, Joint Institute for Regional Earth System Science and Engineering, 607 Charles E Young Drive East, Los Angeles, CA 90095, USA

ARTICLE INFO

Article history:
Received 10 June 2017
Received in revised form 15 October 2017
Accepted 23 November 2017
Available online 23 November 2017
This manuscript was handled by Tim R. McVicar, Editor-in-Chief, with the assistance of Dawen Yang, Associate Editor

Keywords:
Evapotranspiration
Air temperature
Snow
Integrated watershed model
Space-for-time substitution
Soil properties

ABSTRACT

Changes in long-term, montane actual evapotranspiration (ET) in response to climate change could impact future water supplies and forest species composition. For scenarios of atmospheric warming, predicted changes in long-term ET tend to differ between studies using space-for-time substitution (STS) models and integrated watershed models, and the influence of spatially varying factors on these differences is unclear. To examine this, we compared warming-induced (+2 to +6 °C) changes in ET simulated by an STS model and an integrated watershed model across zones of elevation, substrate available water capacity, and slope in the snow-influenced upper San Joaquin River watershed, Sierra Nevada, USA. We used the Soil Water and Assessment Tool (SWAT) for the watershed modeling and a Budyko-type relationship for the STS modeling. Spatially averaged increases in ET from the STS model increasingly surpassed those from the SWAT model in the higher elevation zones of the watershed, resulting in 2.3–2.6 times greater values from the STS model at the watershed scale. In sparse, deep colluvium or glacial soils on gentle slopes, the SWAT model produced ET increases exceeding those from the STS model. However, watershed areas associated with these conditions were too localized for SWAT to produce spatially averaged ET-gains comparable to the STS model. The SWAT model results nevertheless demonstrate that such soils on high-elevation, gentle slopes will form ET "hot spots" exhibiting disproportionately large increases in ET, and concomitant reductions in runoff yield, in response to warming. Predicted ET responses to warming from STS models and integrated watershed models may, in general, substantially differ (e.g., factor of 2–3) for snow-influenced watersheds exhibiting an elevational gradient in substrate water holding capacity and slope. Long-term water supplies in these settings may therefore be more resilient to warming than STS model predictions would suggest.

© 2017 Elsevier B.V. All rights reserved.

1. Introduction

Snowmelt-derived streamflow from mountain watersheds is a critical water source for ecosystems worldwide (Barnett et al., 2005). Snowmelt runoff is particularly important in Mediterranean climates such as the Sierra Nevada of California, where approximately 80–90% of precipitation occurs between late fall (November) and early spring (April) (Pandey et al., 1999). Changes in climate in the western U.S. since the 1970s have shortened snowmelt seasons (Harpold et al., 2012) and advanced streamflows earlier in the year by as much as four weeks (Dettinger et al., 2004; Stewart et al., 2005; Clow, 2010). Observed components of climate change include atmospheric warming (Cayan et al., 2008; IPCC, 2014) and its relationship with precipitation intensity (Lenderink and van Meijgaard, 2008; Westra et al., 2013, 2014), as well as wind speed (McVicar et al., 2010, 2012; Luce et al., 2013), radiative fluxes (Wild, 2009; Milly and Dunne, 2011), and atmospheric aerosols and gases (Milly and Dunne, 2016; Trancoso et al., 2017). Atmospheric warming is especially relevant in assessments of

* Corresponding author at: University of Nevada, Global Water Center, 1664 N. Virginia St, Reno, NV 89557, USA.
E-mail addresses: sjepsen@unr.edu (S.M. Jepsen), tharmon@ucmerced.edu (T.C. Harmon), dficklin@indiana.edu (D.L. Ficklin), noah.molotch@colorado.edu (N.P. Molotch), bin.guan@jpl.nasa.gov (B. Guan).

https://doi.org/10.1016/j.jhydrol.2017.11.042
0022-1694/© 2017 Elsevier B.V. All rights reserved.

snowmelt runoff because of its known control on the partitioning of precipitation between snow and rain (Klos et al., 2014; Safeeq et al., 2016). Projected global changes in air temperature from global climate models (GCMs) tend to be consistent in direction (but not magnitude), ranging from 0.3 to 4.8 °C by year 2100, relative to 1986–2005, depending on greenhouse gas emissions (IPCC, 2014). Cayan et al. (2008) reported a similar amount of warming possible for California (i.e., 1.5–4.5 °C by 2100) using two GCMs and two emission scenarios. In contrast to air temperature, GCM-projected changes in precipitation for California are not consistent in direction (Ficklin et al., 2012; Seager et al., 2013), mainly due to varied representations of extreme precipitation events (Pierce et al., 2013). A potential hydrologic impact of future atmospheric warming will be a shift in timing of the stream hydrograph by as much as six weeks depending on changes in snowfall-rainfall partitioning and snowmelt timing (Null et al., 2010; Costa-Cabral et al., 2013; He et al., 2013). This could lead to increased flooding (Miller et al., 2003; Westra et al., 2014) and increased stresses on ecosystems in association with reduced summertime soil moisture and baseflows (Tague et al., 2009; Godsey et al., 2014). Another potential hydrologic impact of atmospheric warming, addressed in this study, is long-term change in streamflow volume (runoff yield). Previous studies have reached different conclusions regarding the sensitivity of long-term runoff yield to air temperature (Duell, 1994; Risbey and Entekhabi, 1996; Jeton and Dettinger, 1996; Dettinger et al., 2004; Costa-Cabral et al., 2013; He et al., 2013; Goulden and Bales, 2014, Berghuijs et al., 2014, Barnhart et al., 2016). Though reasons for this are not clear, they likely include differences in prediction method, climate, and landscape characteristics.

Models used in previous studies to assess the sensitivity of long-term runoff yield to air temperature can be broadly divided into two categories (Vicuna and Dracup, 2007): (i) empirical models built entirely from statistical relationships trained to observations, and (ii) integrated watershed models that include some aspect of physically based algorithms describing water flows and water demands (e.g., Darcy's Law, Penman-Monteith equation). Of the former category, space-for-time substitution has been a commonly used approach (Hunsaker et al., 2012; Berghuijs et al., 2014; Goulden and Bales, 2014; Reinfelds et al., 2014), whereby empirical models are trained to observations distributed over space to predict a system response with respect to time. In one example, Goulden and Bales (2014) used long-term values of air temperature, precipitation, and MODIS-derived evapotranspiration (ET) sampled across different elevations ("space-") of a mountain watershed to train a regression model to predict temporal responses of long-term runoff and ET to warming in each elevation band of that watershed. A limitation of the space-for-time substitution approach is that it does not take into account independent changes in the spatially varying factors being considered in a system (e.g., components of climate change listed in Section 1).

Long-term changes in ET and runoff yield can be related to one another because of the diminished role of water-storage change over extended time periods. This relationship can be considered in the context of the following water balance:

$$Q/A = P - ET - \Delta S/\Delta t, \quad (1)$$

where Q/A is stream discharge normalized by upstream contributing area (mm yr^{-1}), P is precipitation (mm yr^{-1}), and $\Delta S/\Delta t$ is rate of change in storage (mm yr^{-1}). When this water balance expression (Eq. (1)) is averaged over several years or more, the storage-change term becomes relatively insignificant (Peters and Aulenbach, 2011; Goulden et al., 2012), leading to the following long-term approximation:

$$\Delta(Q/A) = \Delta P - \Delta ET. \quad (2)$$

Previous studies using integrated watershed models have generally predicted more muted long-term responses of ET and runoff yield to warming than studies using space-for-time substitution models (Jepsen et al. 2016; Supplement Section S1). Such muted responses of ET and runoff yield to warming in snow-influenced watersheds are consistent with the concept that advances (earlier shifts) in timing of the stream hydrograph caused by snow-to-rain transitions tend to mute, or offset, responses of stream volume to warming as a result of increased water-limitations on ET (Jeton and Dettinger, 1996; Risbey and Entekhabi, 1996; Dettinger et al., 2004; Tague et al., 2009). Increased water limitations on ET would in general be maximized by reducing soil moisture most during times when potential ET is greatest. Such a reduction in moisture could be brought about by changes in flow path of runoff (e.g., increased overland flow) and/or asynchronous changes in the seasonal timing of surface-water delivery (rainfall + snowmelt) and potential ET. Jepsen et al. (2016) showed that water limitations on ET in response to a snow-to-rain transition are strongly mediated by hydrogeologic conditions that vary with elevation (Jepsen et al., 2016). It is understood that subsurface properties influencing storage capacity, subsurface residence time, and flow velocity play an important mediating role in the effect of interannual climate variability on annual fluxes of ET and runoff (Milly, 1994; Merz and Blöschl, 2009; Lundquist and Loheide, 2011; Troch et al., 2013, Tague and Peng, 2013; Garcia and Tague, 2015). Improved understanding is needed, however, on how shifts from snow to rain, soil/regolith properties, and topography interact to mediate long-term responses of runoff yield and ET to changes in air temperature. Such an improved understanding would provide useful insights into potentially differing responses of runoff yield and ET to atmospheric warming across mountain landscapes, and also about the environmental conditions amenable to a correspondence between predictions from integrated watershed models and space-for-time substitution models.

Our goal is to understand the influence of landscape characteristics in snow-influenced watersheds on the sensitivity of long-term ET to air temperature. Landscape characteristics examined here are the capacity of substrates to store water for plants (available water capacity), ground slope, and elevation. These are hypothesized to be important factors linking changes in long-term energy- and water-availability to changes in actual ET. More specifically, our objectives are two-fold: (1) to simulate and analyze, using an integrated watershed model, variations in warming-induced, long-term change in ET across different zones of substrate available water capacity (AWC), slope, and elevation; and (2) to identify the above landscape characteristics for which there is, and is not, a correspondence between predictions from the integrated watershed model and a space-for-time substitution model. This work provides an improved understanding of how landscape characteristics mediate long-term responses of ET to warming in snow-influenced watersheds, and the landscape characteristics conducive to a correspondence between predictions from integrated watershed models and space-for-time substitution models.

2. Study area

The study area is the upper San Joaquin River watershed in the central Sierra Nevada of California, extending from the crest of the Sierra Nevada Range southwest to the Friant Dam stream gauge below Millerton Lake (Fig. 1). Elevations in the watershed range from 90 to 4210 m across a total area of 4347 km^2. Slopes in the watershed increase moderately with elevation, from an average of 13° in the lower elevation subbasins to 21° in the upper elevation subbasins (Fig. 1). The watershed is divided into four groups of subbasins based on their mean elevations (Table 1).

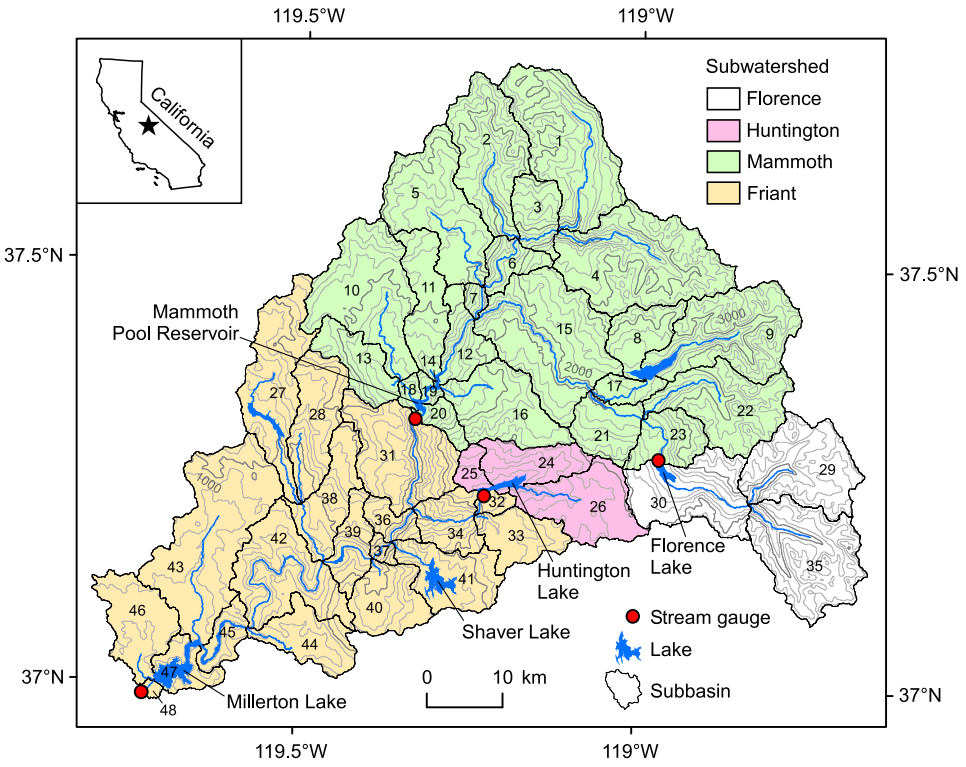

Fig. 1. Location of study area in the upper San Joaquin River watershed, California, USA. Subwatersheds (shaded in color) consist of subbasins (outlined and numbered) that contribute runoff to each of the stream gauges shown. Topography is shown with a 200-m contour interval and was obtained from the USGS National Elevation Dataset (USGS, 2013). Water bodies are based on the USGS National Hydrography Dataset (USGS, 2014b).

These subbasin groups are approximately equal in total area, and are hereafter referenced by their elevation bin (e.g., upper elevation bin).

The watershed is in a Mediterranean climate where approximately 76% of annual precipitation (946 mm yr^{-1}) occurs during the months of November through March, based on 1950–1999 interpolated observations from Maurer et al. (2002) (Table 1). Precipitation increases from approximately 690 mm yr^{-1} in the lower elevations to 1080 mm yr^{-1} in the upper elevations (Table 1). Mean annual air temperature spatially averaged over the watershed is 7.1 °C, and is 0.8 °C during the November through March wet season (Table 1). The rain-snow transition zone is where precipitation typically occurs as a mix of rain and snow in a proportion that is sensitive to air temperature. Based on typical wet-season air temperatures, and a typical snow-to-rain transition range of −2 to 4 °C (Dai, 2008), the rain-snow transition zone is located primarily in the mid-lower elevation bin of the watershed (i.e., subbasins with 1560–2210 m mean elevation). A nearby example of a catchment in the rain-snow transition zone is the P301 experimental catchment (1950 m mean elevation) located 10 km southeast of

Table 1
Definitions and characteristics of four elevation bins dividing the watershed into approximately equal areas. Each elevation bin consists of all subbasins with mean elevations within the elevation range for that bin. Air temperature (T) and precipitation (P) are mean annual values during 1950–1999 from Maurer et al. (2002). AWC = available water capacity averaged over soil and exposed bedrock. All values are spatial averages. Land cover data on last five rows are from NLCD 2001 (USGS, 2014a). Soil and bedrock data are from the STATSGO soil database (USDA, 1994) packaged with ArcSWAT for SWAT2012 (Winchell et al., 2013).

Quantity	Upper bin	Mid-upper bin	Mid-lower bin	Lower bin
Elevation range (m)	2800–3420	2210–2800	1560–2210	130–1560
Subbasin numbers	4, 8, 9, 22, 29, 30, 35	1, 2, 3, 5, 16, 17, 21, 23, 24, 25, 26, 33	6, 7, 10, 11, 12, 13, 15, 20, 28, 31, 32, 34, 41	14, 18, 19, 27, 36, 37, 38, 39, 40, 42, 43, 44, 45, 46, 47, 48
Elevation, mean (m)	3125	2576	1879	844
Area (%)	24.2	25.7	25.4	24.7
P (mm yr^{-1})	1082	1049	957	694
P (%) during Nov 01–Mar 31	73%	76%	77%	79%
T (°C)	1.6	4.3	8.2	14.2
T (°C) during Nov 01–Mar 31	−4.8	−1.8	2.3	7.6
Soil/exposed bedrock	9%/91%	43%/57%	71%/29%	100%/0%
AWC (mm H_2O)	27	58	90	145
Slope (deg)	21	16	16	13
Evergreen forest (%)	32	59	70	51
Shrub/scrub (%)	25	26	26	18
Barren land (rock/sand/clay) (%)	33	11	1	0
Grassland/herbaceous (%)	7	2	1	26
Other land cover (%)	3	2	2	5

Shaver Lake (Fig. 1), where 35–60% of precipitation fell as snow during 2004–2007 (Hunsaker et al., 2012).

The lower elevations of the watershed are covered primarily by sandy loam soils of the Ahwahnee and Holland soil series, while the upper elevations are covered primarily by exposed bedrock and sparse patches of sandy loam soils of the Notned and Gerle soil series (Supplement Fig. S1). Exposed bedrock covers an order of magnitude more area than soil in the upper elevation bin of the watershed (Table 1). A soil map with brief descriptions are given in Supplement Fig. S1 and Table S1, with more detailed descriptions available at https://soilseries.sc.egov.usda.gov/. The dominant land cover types in the watershed are evergreen forest (53%) and shrubland/scrubland (24%) (USGS, 2014a) (Table 1). The evergreen forest consists of ponderosa pine, sugar pine, white fir, and incense cedar at elevations below approximately 2000 m (Giger and Schmitt, 1993). This forest transitions into white fir, red fir, Jeffrey pine, lodgepole pine, western white pine, and mountain hemlock at higher elevations. The shrublands/scrublands typically include oak, Ceanothus, manzanita, and buckeye. Grasslands are common in the lowest elevations and in high-elevation meadows (Table 1).

Streamflows in the watershed are heavily regulated for hydropower, flood control, and instream flow requirements (MAH, 2003). The watershed contains nine dams built between 1910 and 1960, impounding all of the lakes mapped in Fig. 1. Stream gauges used in this study are located below dams at Florence Lake, Huntington Lake, Mammoth Pool Reservoir, and Millerton Lake (Friant Dam). Based on these stream gauge locations, we divided the watershed into four subwatersheds for purposes of hydrologic modeling. In order of decreasing mean elevation, these subwatersheds are: Florence, Huntington, Mammoth, and Friant (Fig. 1, Supplement Table S2). Simulation of all historical reservoir operations are beyond the scope of this study. Therefore, all streamflows used and presented in this study are "full natural" ("unimpaired") values, which are best estimates by operating agencies of the flows that would have occurred in the absence of regulations. Mean annual streamflow during 1960–1979, normalized by upstream contributing area (Supplement Table S2), ranged from 485 mm yr^{-1} at the Friant Dam stream gauge (http://cdec.water.ca.gov/cgi-progs/queryCSV, station ID# SJF, sensor# 65) to 670 mm yr^{-1} at the Florence Lake stream gauge (http://cdec.water.ca.gov/cgi-progs/queryCSV, station ID# SFR, sensor# 65).

3. Methods

3.1. Overview of experiment design

We simulated changes in long-term ET in response to three incremental shifts in air temperature applied to a 20-yr baseline climate (1960–1979): 0 (baseline) to +2 °C, +2 to +4 °C, and +4 to +6 °C. These air temperature shifts were applied uniformly to air temperatures of the baseline climate period. In order to examine the cause-effect relationship between warming and long-term ET, and to directly compare our space-for-time substitution results to those from previous studies that considered changes in air temperature (Supplement Section S1), meteorological parameters other than air temperature were maintained at baseline values. The above warming cases bracket a range in potential 21st century warming scenarios based on GCMs and possible greenhouse gas emissions (IPCC, 2014).

We separated outputs of the integrated watershed model into bins of elevation, substrate available water capacity (AWC), and slope. The elevation bins used for results from both the watershed model and space-for-time substitution model were defined in terms of the subbasin groups listed in Table 1. We selected three bins of substrate AWC: "Rock," exposed bedrock which has AWC-values of less than 16 mm H_2O (Supplement Table S1); "AWC-1," soils with 16 mm < AWC $\leq$ 91 mm; and "AWC-2," soils with AWC > 91 mm. The AWC-1 and AWC-2 bins were defined in this manner in order to divide the soils in the upper half of the watershed into approximately equal areas (14% and 15% for AWC-1 and AWC-2, respectively, not shown). We chose three slope bins of 0–20%, 20–40%, and >40% during construction of the watershed model to represent roughly equal areas of the watershed (38%, 25%, and 38%, respectively).

Parameters were input to the integrated watershed model as ranges of values obtained from a calibration procedure using the Sequential Uncertainty Fitting (SUFI-2) method (Abbaspour et al., 2004, 2007) (Section 3.5). Output from the calibrated watershed model was in the form of 1000 time-series simulations at a monthly time-step, enclosing approximately 80–90% of monthly flow observations (Section 4.1). Parameters input to each of these 1000 simulations were obtained from latin-hypercube random sampling of the parameter ranges determined in the calibration procedure (Section 3.5). Simulated changes in mean annual ET were spatially integrated over model Hydrologic Response Units (HRUs), patches of subbasins having a unique combination of land-use, soil type, and slope, using HRU area-weighting. This was done over the HRUs in each bin of elevation, substrate AWC, and slope. Following Abbaspour et al. (2004, 2007), we defined the prediction uncertainty as the range between the 2.5- and 97.5-percentiles of the 1000 watershed model simulations, and the mean simulation as the average over this range of uncertainty.

3.2. Watershed model

Our criteria for selecting a watershed model was that it should simulate relevant hydrologic processes using physically based relationships and, from a more pragmatic standpoint, that it should be supported by documentation, user groups, and pre- and post-processing software tools. One relevant hydrologic process is a shift from snowfall to rainfall with increased air temperature, as this can influence the long-term water balance through asynchronous changes in timing of water availability and water demand (Milly, 1994; Tague et al., 2009). Another relevant process is how changes in timing and intensity of surface water flux (rainfall and snowmelt) affect the dynamics of soil moisture and flow paths of runoff, which include infiltration, overland flow, interflow, and percolation through soil. This interaction plays an important role in the availability of subsurface water during the growing season (Milly, 1994; Merz and Blöschl, 2009; Lundquist and Loheide, 2011; Troch et al., 2013, Tague and Peng, 2013; Garcia and Tague, 2015). Based on these considerations, we selected the SWAT version 2012 (revision 632) watershed model, with the ArcSWAT extension tool for ArcGIS (version 2012.10_2.16) for building the model in ArcMap (Arnold et al., 2012; Winchell et al., 2013). Previous studies have demonstrated that SWAT can effectively capture the dynamics of runoff from snow-influenced mountain watersheds (Fontaine et al., 2002; Ahl et al., 2008; Zhang et al., 2008; Ficklin et al., 2012; Watson and Putz, 2014; Grusson et al., 2015).

In SWAT, a snowpack accumulates when new precipitation occurs while air temperature is below a threshold value, and melts according to a calibrated model that uses melt factors and multiple elevation bands per subbasin (Fontaine et al., 2002). We applied five elevation bands per subbasin based on cumulative hypsometric curves of elevation. Snowmelt fluxes in the elevation bands are adjusted for a non-uniform snow distribution using a sigmoidal areal depletion curve that relates areally averaged snow water equivalent to fractional snow covered area (Fontaine et al., 2002; Neitsch et al., 2011). Partitioning between infiltration and surface runoff was computed using the SCS (Soil Conservation Service)

curve number method, which adjusts land-use specific, daily infiltration volumes based on local values of soil layer permeability, antecedent soil moisture, and slope (Neitsch et al., 2002; Supplement Section S2). Water within a soil profile can flow laterally as interflow along soil layers that become saturated, can percolate vertically downward when soil water content exceeds field capacity, and can be uptaken by plant roots. Water percolating out of the soil column is time-lagged across the vadose zone to eventually recharge an aquifer, which provides base flow to a stream reach following a linear reservoir model (Neitsch et al., 2002). Water can be lost from the watershed as deep aquifer recharge, which we left at the model's default value of 5% total aquifer recharge. We selected the Penman-Monteith method for computing potential ET. Components of potential ET influenced by air temperature are net shortwave and longwave radiation, and vapor pressure gradient. Net shortwave radiation was corrected for a surface albedo of 0.8 when a snow cover is present, and an area-weighted average for soil and vegetation at other times (Neitsch et al., 2011, p. 36). Net longwave radiation was computed using a modified version of the Stefan-Boltzmann law to account for vapor pressure effects on atmospheric emittance (Neitsch et al., 2011, p. 37–38). Aerodynamic resistances in the Penman-Monteith equation were parameterized by canopy height, and canopy resistance to vapor flux was parameterized by leaf area index (Neitsch et al., 2011, p. 127–128). If soil water storage is insufficient to meet ET demands, water is extracted directly from the aquifer in a flux referred to as REVAP. This flux is intended to simulate water uptake by deep plant roots and/or upward capillary flow from shallow water tables (Neitsch et al., 2002). Water storages and fluxes in SWAT are evaluated for each HRU, then routed to stream reaches.

3.3. Space-for-time substitution model

There is no singly accepted space-for-time substitution (STS) method for predicting a change in long-term ET or runoff. Methods from previous studies have included the use of a linear relationship between runoff ratio and elevation in conjunction with an elevation-air temperature lapse-rate (Hunsaker et al., 2012; Reinfelds et al., 2014), use of nonlinear regression between long-term ET, air temperature, and precipitation (Goulden et al., 2012; Goulden and Bales, 2014), and use of a Budyko-type relationship (Berghuijs et al., 2014) between long-term evaporation ratio, ET/P, and aridity ratio, PET/P, where P is mean annual precipitation and PET is mean annual potential ET (Budyko, 1974, pp. 317–330; Zhou et al., 2015). A method common to these studies (including ours) is the use of long-term annual averages, which does not explicitly account for seasonal variability in factors such as temperature lapse-rate (e.g., McVicar et al., 2007). Similar to the approach by Berghuijs et al. (2014), we assumed that long-term ET in each subbasin of the watershed (Fig. 1) follows a Budyko-type relationship between evaporation ratio and aridity ratio. In addition, we assumed temporal stationarity in the following two lapse rates: mean annual air temperature versus elevation based on interpolated COOP station observations (Maurer et al., 2002) during the 1960–1979 baseline period, -5.2×10^{-3} °C m^{-1} (Fig. 2a), and mean annual potential ET versus elevation during the baseline period, -0.365 mm yr^{-1} m^{-1} (Fig. 2b). Potential ET was computed using the Penman-Monteith method with the same meteorological data used for SWAT (Section 3.4). Mean annual ET for the Budyko-plot ordinates (Fig. 2c) were estimated as the difference between precipitation and observed, net stream discharge from each subwatershed during the 1960–1979 baseline period (Supplement Table S2).

In selecting the functional form of the Budyko-type relationship, we tested all functions in Zhou et al. (2015) and chose their Eq. (23a) because it provided the best fit ($R^2 = 0.92$) to our subwatershed data points (Fig. 2c). To make an ET-change prediction using the STS model, we first multiplied the prescribed shift in air temperature by the reciprocal of the air temperature lapse-rate, -192 m °C^{-1}, to produce an equivalent change in elevation. We then multiplied this equivalent change in elevation by the potential ET lapse-rate (-0.365 mm yr^{-1} m^{-1}) to produce an equivalent change in potential ET. Lastly, we inserted this equivalent change in potential ET into the Budyko-type relationship (Fig. 2c) to predict the corresponding change in long-term ET. This method used elevation as an intermediate parameter relating a change in air temperature to a corresponding change in potential ET. Another method, yielding the same result, would have been to parameterize potential ET by air temperature (70.6 mm yr^{-1} °C^{-1}, $R^2 = 0.93$, Supplement Fig. S2) rather than elevation.

3.4. Model inputs

Each subbasin in SWAT is assigned a single gauge providing meteorological time-series data. For air temperature and precipitation, we used daily values from the gridded (1/8°) product of Maurer et al. (2002) mapped from NOAA COOP station observations. We projected grid cell values to each subbasin by area-weighting overlaps between grid cells and subbasins (average grid cell area = 154 km^2, average subbasin area = 91 km^2). Other daily meteorological forcings needed for the potential ET calculations – solar radiation, relative humidity, and wind speed – were generated internally in SWAT using the WXGEN weather generator parameterized by first-order climate stations in the U.S. (Neitsch et al., 2011). The same subbasin values of air temperature, precipitation, and potential ET were used in both the SWAT model and STS model. Ground surface elevations were obtained from a 1-arcsecond digital elevation model of the National Elevation Dataset (USGS, 2013).

To constrain the calibration ranges of the watershed model parameters controlling the sigmoidal shape of the snow areal depletion curve (SWAT parameters SNOCOVMX and SNO50COV), we used the satellite-based, blended snow reconstruction product from Guan et al. (2013) (Fig. 3). Substrate (i.e., soil and exposed bedrock) properties input to ArcSWAT were obtained from the USDA State Soil Geographic (STATSGO) database (USDA, 1994) (Supplement Fig. S1 and Section S2). Land cover ("land use" in SWAT) data input to ArcSWAT were obtained from the National Land Cover Database 2001 (USGS, 2014a). The land cover types represented in the watershed model were evergreen forest, shrubland/scrubland, grassland/herbaceous plants, and barren land, covering 95% of the watershed (Table 1). Other more minor land covers, covering less than the default threshold of 20% any given subbasin, were screened out during HRU creation in ArcSWAT (Winchell et al., 2013, p. 122).

3.5. Watershed model calibration and sensitivity analysis

We applied a calibration procedure to the watershed model consisting of adjustments to the most important parameters to match simulated and observed streamflows as closely as possible (Santhi et al., 2001). To identify the most important model parameters, we compiled from the literature a list of 26 commonly adjusted parameters and their estimated ranges of uncertainty (Supplement Table S3). Next, we evaluated the relative importance of each parameter by applying a global sensitivity analysis using the Sobol' method, which apportions the variance in an arbitrary model response to each parameter (Saltelli et al., 2008, pp. 159–167) (Supplement Section S3). The model responses examined in this analysis were the Nash-Sutcliffe coefficient (Nash and Sutcliffe, 1970), NS, and model percent bias, PB, equal to the

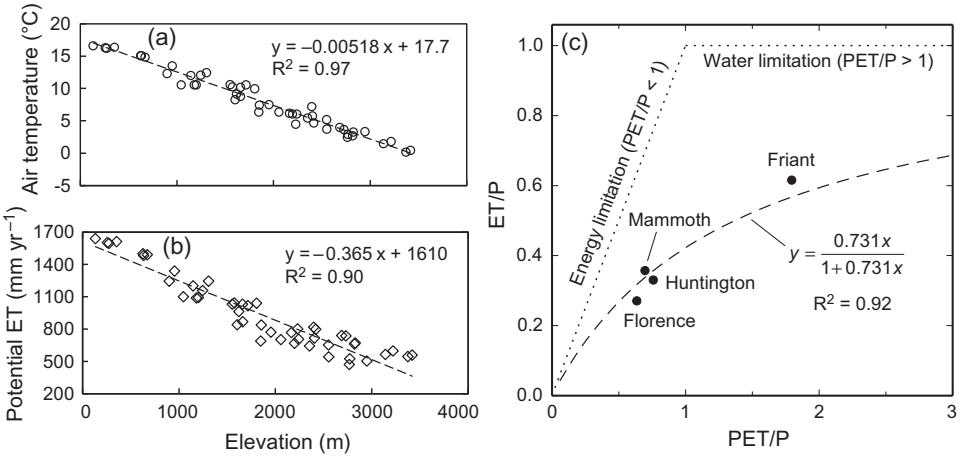

Fig. 2. Relationships used in the space-for-time substitution (STS) model to predict long-term increases in evapotranspiration (ET) in response to warming. (a) Subbasin-averaged values of mean annual air temperature versus mean elevation. (b) Subbasin-averaged values of mean annual potential ET versus mean elevation. (c) Budyko-type relationship between evaporation ratio (ET/P) and aridity ratio (PET/P). Dashed line shows best fit of subwatershed data points to Eq. (23a) in Zhou et al. (2015). Subwatershed ET-values (points) were estimated as the long-term difference between annual precipitation and net stream outflow normalized by contributing area (Supplement Table S2). Potential ET are mean simulated values from the SWAT model, air temperature and precipitation are interpolated observations from Maurer et al. (2002). All quantities are averages during the 1960–1979 baseline period.

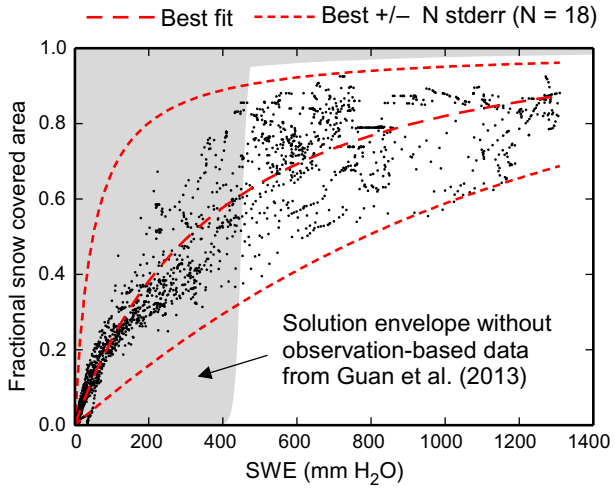
Best fit
Best +/– N stderr (N = 18)
Fractional snow covered area
Solution envelope without observation-based data from Guan et al. (2013)
SWE (mm H2O)

Fig. 3. Data used to constrain the calibration ranges of SWAT model parameters (SNOCOVMX and SNO50COV) controlling the sigmoidal shape of the areal depletion curve relating fractional snow covered area to snow water equivalent (Fontaine et al., 2002). Plotted points are from the daily snow reconstruction product from Guan et al. (2013) averaged over watershed elevations above 2000 m during 01 March 2000 to 31 August 2014. Gray-shaded region is the envelope of curves for typically used parameter ranges of 1–500 mm for SNOCOVMX and 0.05–0.9 for SNO50COV, ranges that we would have used without the Guan et al. (2013) dataset. Long-dashed line shows best fit of the data points to the areal depletion curve given by Eqs. (8) and (9) in Fontaine et al. (2002). The optimum values (standard errors) of parameters for the best fit are 2390 mm (74.9 mm) for SNOCOVMX, and 0.129 (0.00452) for SNO50COV. Short-dashed lines are the areal depletion curves with parameters SNOCOVMX and SNO50COV offset from optimum values by N standard errors, with N chosen to be 18 in order to bracket 95% of the data points. Based on these results, the calibration ranges were found to be 1038–3735 mm for SNOCOVMX, and 0.0473–0.210 for SNO50COV.

percent error in modeled streamflow volume (positive for model overestimates). Based on results of the sensitivity analysis, we selected the 20 model parameters accounting for 99% of total model variance in NS and PB (Fig. 4, filled symbols) and included these in the set of parameters to adjust in model calibration. We noted the following observations from the sensitivity analysis results: (i) the seven snow parameters of the model (Supplement Table S3) accounted for most (78%) of the variance in NS, (ii) more parameters were needed to account for a given variance in PB than NS (e.g., four parameters for ~80% of NS variance compared to seven parameters for PB) (Fig. 4), and (iii) one of the parameters (SNO50COV) controlling the sigmoidal shape of the snow areal depletion curve, constrained using the Guan et al. (2013) dataset (Fig. 3), was the second most influential parameter in terms of modeled streamflow volume (Fig. 4, bottom).

We calibrated the watershed model to the 1955–1967 period of observed, monthly, full natural streamflow, using 1950–1954 for spin-up initialization of model states. Calibrated models were then evaluated using 1968–1979 observations (using 1963–1967 for spin-up). These time periods were selected based on the availability of the meteorological dataset starting in 1950 and the availability of data at all stream gauges until the end of 1979. The temporal misalignment between the SWAT-input datasets for meteorology (1955–1979) and land cover (circa 2001) are not likely an issue as land cover change in the vicinity of the study area has been minor since at least the 1980s (Potter, 2015).

To calibrate the watershed model, we used the Sequential Uncertainty Fitting algorithm (SUFI-2) calibration and uncertainty tool of the SWAT-CUP software package (Arnold et al., 2012). In each manual iteration of SUFI-2, parameter ranges are contracted by amounts depending on the parameter covariance matrix, while being centered about the parameters of the "best simulation" (Abbaspour et al., 2004, 2007; Yang et al., 2008). The best simulation was the one producing the best goal function (i.e., objective function), defined to be NS in this study. SUFI-2 iterations were repeated until the "r-factor" was reduced to a value of approximately one. The r-factor in SUFI-2 is defined as the temporally averaged width of the 2.5- to 97.5-percentile ranges of model output (i.e., the 95% prediction uncertainty range), normalized by the standard deviation of the measured data (Supplement Section S4). The goal of the SUFI-2 calibration procedure is to bracket as many measurements as possible in the 95% prediction uncertainty range, a fraction referred to as the "p-factor." In addition, the statistics NS, R^2, and PB for the best model simulation should be in acceptable ranges. We defined four levels of model performance – "very good", "good", "fair", and "poor (unacceptable)" – for the p-factor, NS, R^2, and PB statistics based on conventions from previous studies (Supplement Table S4). We calibrated the watershed model two different ways. For the "globally" calibrated model, we adjusted all parameters uniformly across the watershed using only

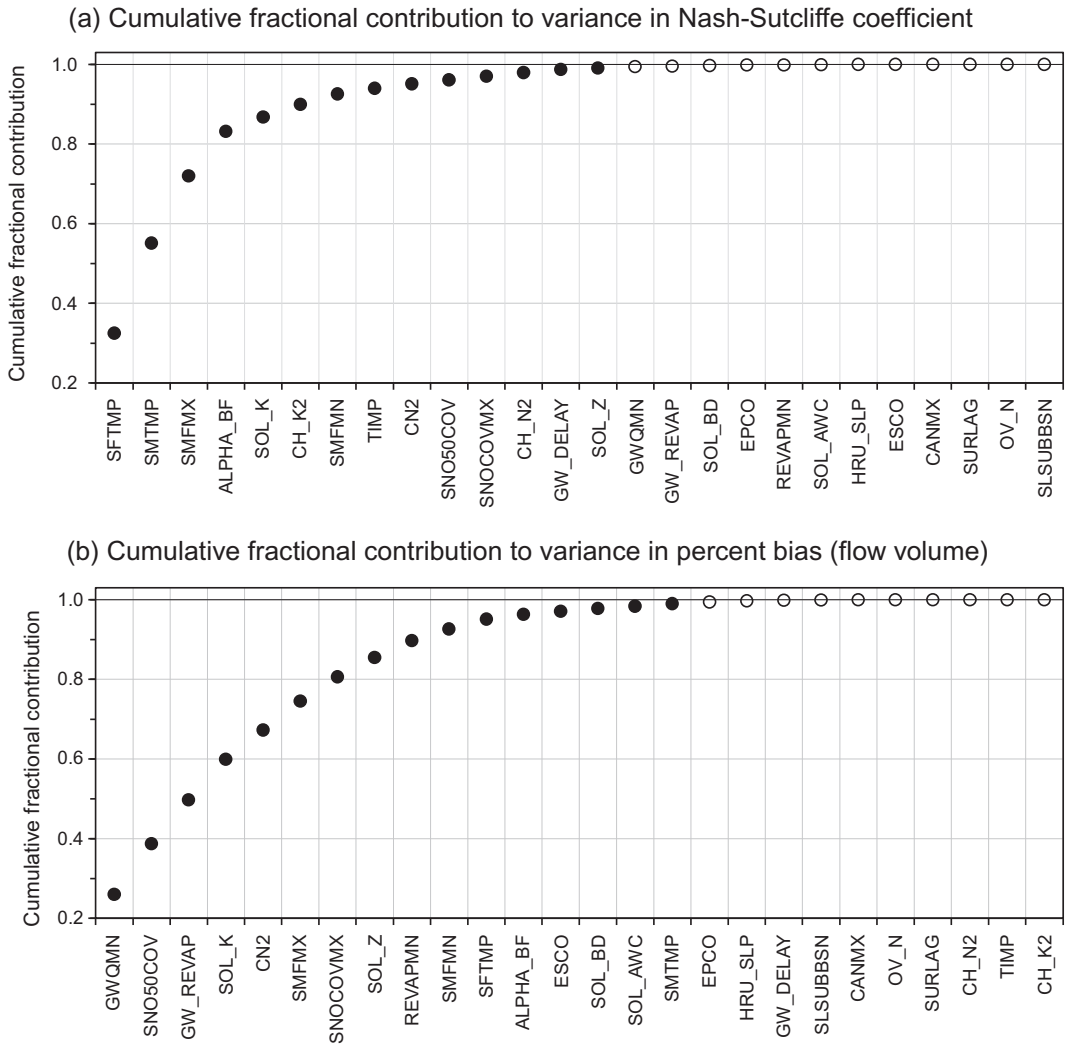

Fig. 4. Contributions of individual parameters to the total SWAT-modeled variance in (a) Nash-Sutcliffe coefficient (NS) and (b) model percent bias (PB). Results obtained from a Sobol' (global) sensitivity analysis (Saltelli et al., 2008, pp. 159–167) implemented in the Sensitivity Analysis Library in Python (SALib) (Herman and Usher, 2017). Parameters are described in Supplement Table S3.

measurements at the Friant Dam stream gauge to compute the goal function. For the "locally" calibrated model, we made separate adjustments to the parameters for each subwatershed (Fig. 1) using the stream gauge at the corresponding subwatershed outlet to compute the goal function (see Neitsch et al., 2002, chapter 33; Van Liew et al., 2005). Initial parameter ranges of calibration are listed in Supplement Table S5.

4. Results

4.1. Watershed model evaluation

At the Friant Dam stream gauge, the globally and locally calibrated watershed models showed nearly identical performance in terms of the p-factor (fraction of measurements bracketed) and NS statistic (Table 2, Fig. 5). The p-factors from calibration (validation) of the globally calibrated model, 0.94 (0.90), were similar to values for the locally calibrated model, 0.94 (0.88). The NS-values for the best simulation from calibration (validation) of the globally calibrated model, 0.91 (0.92), were similar to values for the locally calibrated model, 0.90 (0.91). These statistics are all considered to be "very good" (Supplement Table S4). In terms of model percent bias (PB), the globally calibrated model performed slightly better than the locally calibrated model (Table 2), with best simulation values of +7.7 (+2.2) for the globally calibrated model ("good" to "very good") compared to +13.9 (+7.8) for the locally calibrated model ("fair" to "good") (Supplement Table S4). The

Table 2
Performance statistics of the SWAT watershed model for the calibration (validation) periods. Results shown here are for model evaluation at the Friant Dam stream gauge. Time periods are 1955–1967 for calibration, 1968–1979 for validation. The goal function is defined to be the Nash-Sutcliffe coefficient (NS). Definitions: best sim = statistic for the simulation producing the best goal function, mean sim = statistic for the simulation consisting of discharge averages over the 2.5- to 97.5-percentiles for each month, NS = Nash-Sutcliffe coefficient, R^2 = coefficient of determination, PB = model percent bias.

Statistic	Globally calibrated model	Locally calibrated model
p-factor	0.94 (0.90)	0.94 (0.88)
r-factor	1.19 (0.99)	1.15 (0.95)
p/r	0.79 (0.91)	0.82 (0.93)
NS mean sim	0.88 (0.87)	0.89 (0.89)
NS best sim	0.91 (0.92)	0.90 (0.91)
R^2 mean sim	0.90 (0.90)	0.90 (0.92)
R^2 best sim	0.91 (0.93)	0.91 (0.92)
PB mean sim	+9.9 (+5.4)	+12.6 (+7.8)
PB best sim	+7.7 (+2.2)	+13.9 (+7.8)

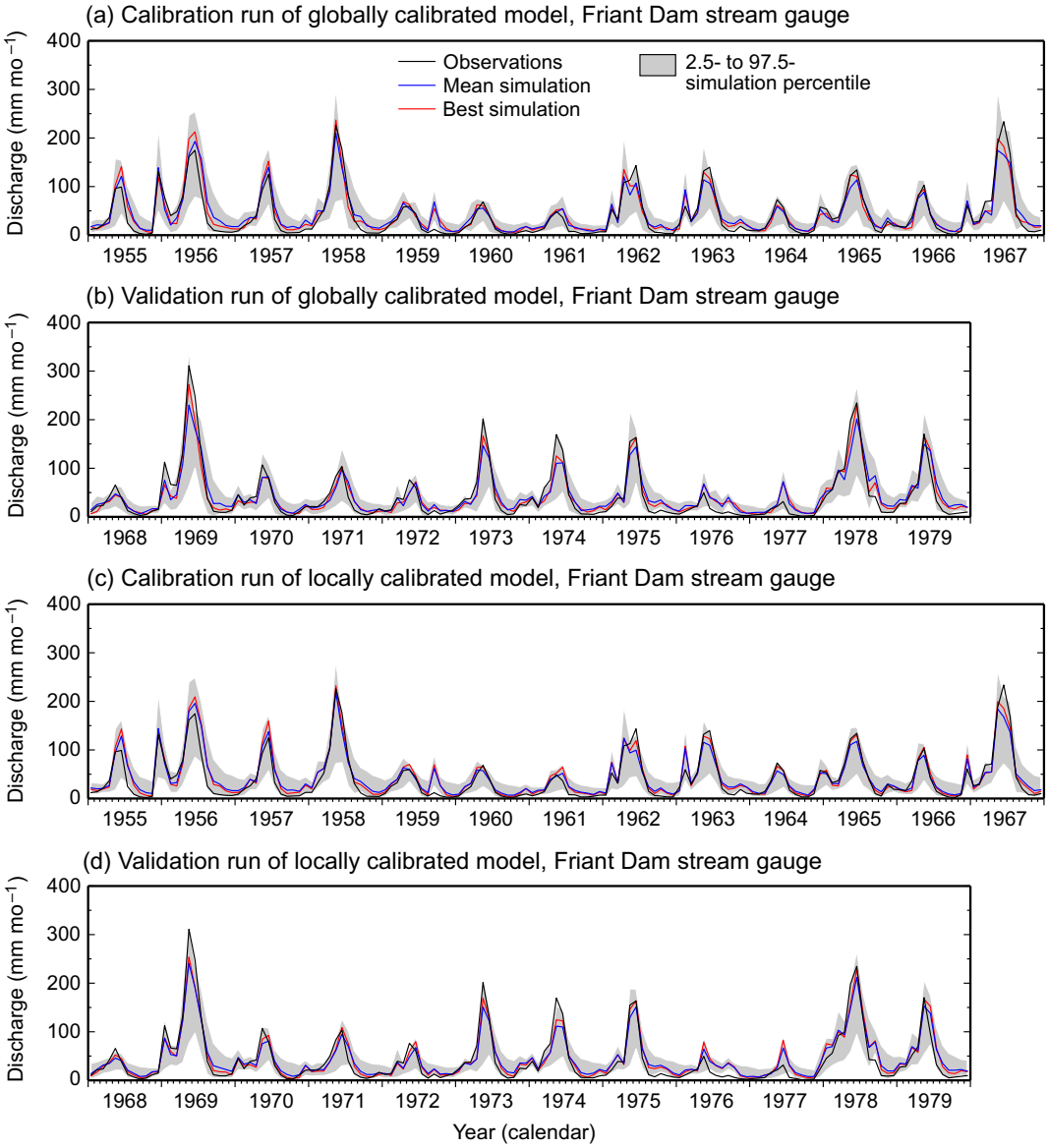
(a) Calibration run of globally calibrated model, Friant Dam stream gauge
Observations
Mean simulation
Best simulation
2.5- to 97.5-simulation percentile
Discharge (mm mo−1)
(b) Validation run of globally calibrated model, Friant Dam stream gauge
(c) Calibration run of locally calibrated model, Friant Dam stream gauge
(d) Validation run of locally calibrated model, Friant Dam stream gauge
Year (calendar)

Fig. 5. SWAT-modeled versus observed monthly stream discharge at the Friant Dam stream gauge during the calibration and validation periods, from (a, b) the globally calibrated model, and (c, d) the locally calibrated model. Gray-shaded regions show the 95% prediction uncertainty ranges defined at the 2.5- to 97.5-simulation percentiles.

final parameter ranges and best-fit parameter values of the globally and locally calibrated models are listed in Supplement Tables S6 and S7, respectively.

At the Florence Lake and Mammoth Pool stream gauges, which collect most high-elevation runoff (Fig. 1), the locally calibrated model did not show a noticeable improvement in performance over the globally calibrated model (Supplement Table S8). This result was somewhat unexpected given that the globally calibrated model was not calibrated to either of these gauges. For example, the p-factors from the validation runs of the globally calibrated model at the Florence Lake and Mammoth Pool stream gauges were 0.74 and 0.83, respectively (Supplement Table S8, upper), compared to values of 0.75 and 0.76 for the locally calibrated model (Supplement Table S8, lower). We did, however, notice an improvement in the locally calibrated model over the globally calibrated model at the Huntington Lake stream gauge in terms of p-factor, NS, and R^2 (Supplement Table S8). However, because this improved performance was limited to a minor (5%) portion of the watershed (Supplement Table S2), we chose to use the simpler globally calibrated model for all of our final warming scenarios. This choice had the effect of retaining the spatial variability originally present in the land cover and soil datasets input to SWAT. The reader is referred to Supplement Figs. S3–S6 for time-series plots of stream discharge at the Florence Lake, Huntington Lake, and Mammoth Pool stream gauges during the calibration and validation periods for both the globally and locally calibrated models.

4.2. Simulated ΔET versus elevation

Simulated ET-changes from the space-for-time substitution (STS) model showed a markedly greater sensitivity to elevation than those from the SWAT watershed model (Fig. 6). STS-modeled values ranged from 17 mm yr^{-1} at the lowest elevations (+5% change from baseline values, Supplement Table S9) to 51 mm yr^{-1} at the highest elevations (+20% change) for the 0–2 °C warming case (Fig. 6a). In comparison, SWAT-modeled values ranged from approximately 20 mm yr^{-1} at the lowest elevations (+5% change) to 18 mm yr^{-1} at the highest elevations (+8% change) for

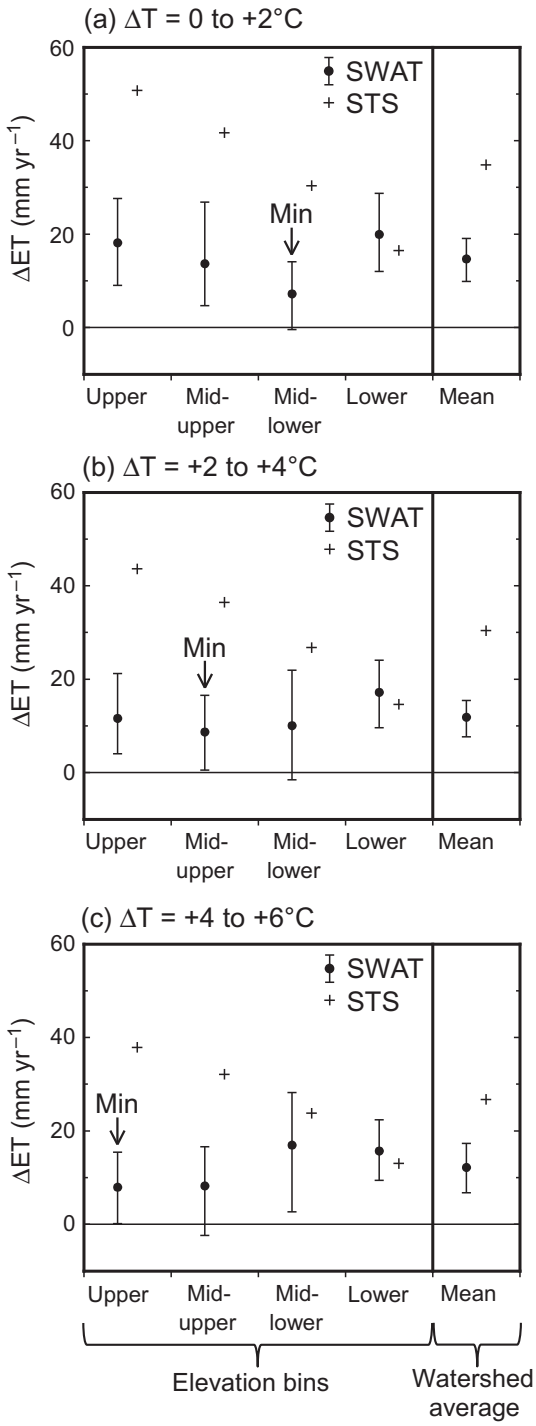

Fig. 6. Simulated changes in mean annual ET from the SWAT watershed model versus the space-for-time substitution (STS) model, spatially averaged over elevation bins and the entire watershed ("Mean"). Results shown for air temperature increases of (a) 0–2 °C, (b) 2–4 °C, and (c) 4–6 °C relative to baseline conditions (1960–1979). Error bars show the prediction uncertainty ranges from SWAT, points in error bars show the mean values in these ranges. Minimum mean values from SWAT are labeled "Min." Elevation bins are defined in Table 1.

the same warming case (Fig. 6a, Supplement Table S9). These model differences in ET-change sensitivity to elevation resulted in a divergence between model predictions with increasing elevation. The maximum differences between model predictions occurred at the highest elevations and were 33 mm yr^{-1} (97% difference) for 0–2 °C warming, 32 mm yr^{-1} (114% difference) for 2–4 °C warming, and 30 mm yr^{-1} (130% difference) for 4–6 °C warming (Fig. 6a–c). This divergence in modeled ET-response to temperature with increasing elevation was associated with monotonic increases with elevation in outputs from the STS model and lack of such monotonicity in outputs from the SWAT model (Fig. 6). The monotonic ET-responses from the STS model followed from the concave-downward shape of the Budyko curve (Fig. 2c), which predicts stronger ET responses to temperature in the more elevated, energy-limited areas of the watershed. This monotonic pattern was not produced in the elevation-binned outputs from the SWAT model.

STS-modeled increases in ET averaged across the watershed ranged from 28 mm yr^{-1} (+8% change, Supplement Table S9) for the 4–6 °C warming case, to 36 mm yr^{-1} (+11% change) for the 0–2 °C warming case (Fig. 6, right). The corresponding predictions from the SWAT model were more muted, ranging from 13 mm yr^{-1} (+4% change) for the 4–6 °C warming case, to 16 mm yr^{-1} (+5% change) for the 0–2 °C warming case (Fig. 6, right). These model differences were driven mainly by differing model responses at higher elevations. In the STS model, the upper elevations of the watershed (i.e., the upper and mid-upper bins) contributed two-thirds of the total volumetric increase in ET (m^3 yr^{-1}) in response to 0–2 °C warming (Fig. 6), with the lower elevations contributing the remaining one-third. In comparison, the upper and lower elevations of the SWAT model contributed similar proportions (54% and 46%) of the increased ET volumes (Fig. 6).

The SWAT simulations revealed elevational zones of minimum ET-increase that migrated to higher elevations with progressive warming. For 0–2 °C warming, this elevational zone occurred in the mid-lower elevation bin (Fig. 6a, "Min"). This elevation bin was noted in Section 2 to be the primary location of the rain-snow transition zone based on historical November–March air temperatures. With progressive warming, the elevational zone of minimum ET-increase migrated to higher elevations, eventually reaching the upper elevation bin for the 4–6 °C warming case (Fig. 6c).

We also observed a scale dependence of prediction uncertainty from the SWAT model. The uncertainties in predicted ET-change at the scale of elevation bins are greater (roughly double) than those at the watershed scale (lengths of bars in Fig. 6). As an example, for the 4–6 °C warming scenario, the 95% prediction uncertainty for the mid-lower elevation bin is 2.5 times greater than for watershed-averaged predictions (Fig. 6c). This scale dependency of uncertainty is presumably associated with our method of spatially integrating model outputs (over HRUs) prior to computing simulation means and prediction uncertainties.

4.3. Simulated ΔET versus substrate, slope, and elevation

Substrate available water capacity (AWC) and slope had a marked influence on ET responses to warming in the SWAT simulations, particularly for the mildest warming at the upper elevations (Fig. 7a, left). Simulated ET responses to 2 °C warming, averaged across slopes of the upper elevation bin, ranged from 15 mm yr^{-1} (+7% change, Supplement Table S10) for exposed bedrock, to 47 mm yr^{-1} (+12% change) for the highest-AWC soils (box averages in Fig. 7a, left). For these soils, nearly half (45%, not shown) of the simulations in the uncertainty range of SWAT exceeded the STS model prediction (Fig. 7a, left). This demonstrates that the SWAT model produces stronger ET responses to warming than the STS model in localized upper-elevation areas with relatively thick soils (Fig. 7d, left). Simulated changes in ET in steeper terrain of the SWAT model tended to be more muted than in gentler terrain, a pattern more apparent at the scale of individual subbasins (Supplement Fig. S7) than elevation bins (Fig. 7).

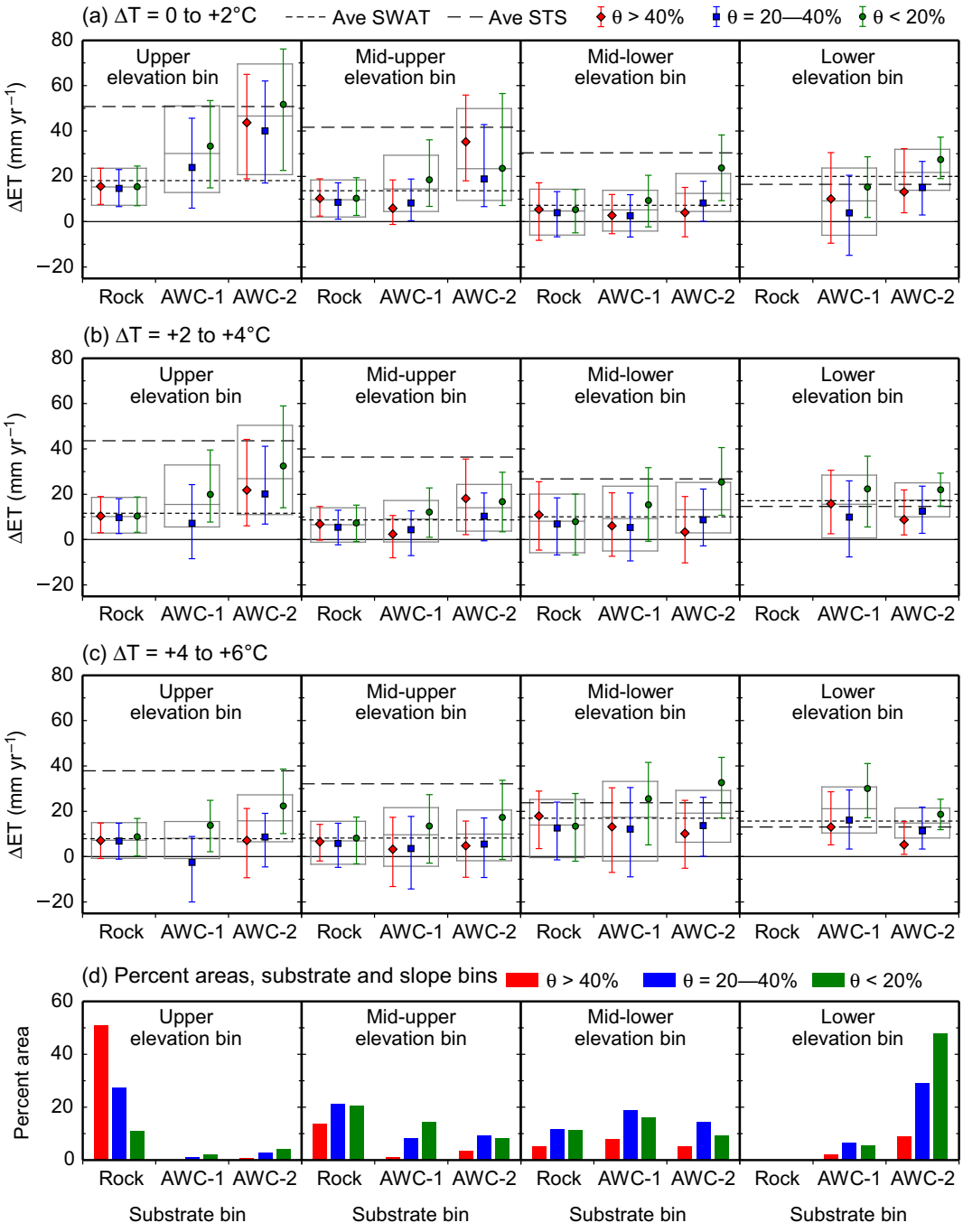

Fig. 7. SWAT-modeled, long-term changes in ET in the different bins of elevation, substrate available water capacity (AWC), and percent slope (θ) for air temperature increases of (a) 0–2 °C, (b) 2–4 °C, and (c) 4–6 °C relative to baseline conditions. Baseline ET-values are listed in Supplement Table S10. Definitions of substrate bins: "Rock," exposed bedrock which has AWC-values < 16 mm; "AWC-1," soils with 16 mm < AWC ≤ 91 mm; and "AWC-2," soils with AWC > 91 mm. (d) Percent land areas in different substrate and slope bins.

Exposed bedrock at high elevations, where increases in ET from SWAT were muted relative to the STS model, occurs in approximately three-fourths of the upper watershed (Table 1). As a result, spatially averaged ET responses from SWAT are substantially lower than predictions from the STS model (Fig. 6). The influence of substrate AWC on predictions from the SWAT model became less pronounced with progressive warming (Fig. 7a–c), an outcome possibly related to increasing water limitations in all substrates as aridity ratios increase (Fig. 2c).

In these constant precipitation experiments, ET reductions in response to warming are an extreme example of increased water limitations caused by earlier seasonal shifts in the timing of water availability (Tague et al., 2009). These types of responses were captured in the prediction uncertainty range of the SWAT model (Fig. 7). Elevational zones where these ET reductions were most pronounced migrated upward with progressive warming, generally following the rain-snow transition zone assuming a phase transition range of −2 to 4 °C (Dai, 2008). For the mildest warming case (0–2 °C), decreases in ET occurred primarily in the lower half of the watershed (Fig. 7a). Further warming resulted in the most pronounced decreases in ET shifting to the upper elevations (Fig. 7c). This upward movement of extreme water-limitation followed the zones of minimum ET-increase mentioned in Section 4.2.

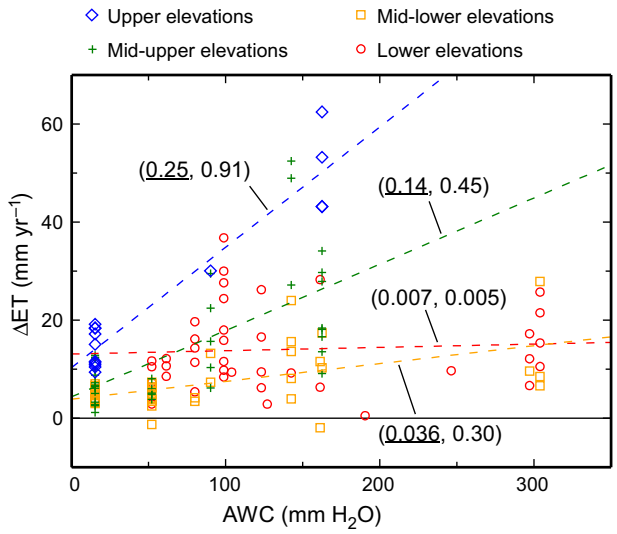

Fig. 8. SWAT-modeled, long-term changes in ET versus substrate available water capacity (AWC) for each elevation bin of the watershed. Results shown for the 0–2 °C warming scenario. Each point represents the area-weighted average for a substrate unit in a subbasin. Dashed lines show results from linear regression applied to data points for each elevation bin, and are labeled with values for trend [underlined if *p*-value < .05 (Student's t-distribution, two-tailed)] and coefficient of determination (R^2). Trends are considered significant (*p*-value < .05) for the mid-lower, mid-upper and upper elevation bins.

Strong interaction between substrate AWC and elevation in the response of long-term ET to warming was supported by a linear regression analysis on SWAT outputs (Fig. 8). This analysis showed that trends between ET-change and substrate AWC strengthened from 0.036 mm yr^{-1} mm^{-1} (R^2 = 0.30, *p*-value < .05) in the mid-lower elevations to 0.25 mm yr^{-1} mm^{-1} (R^2 = 0.91, *p*-value < .05) in the upper elevations. Trends were not statistically significant (*p*-value > .05) in the lowest elevations.

For the mildest warming case (0–2 °C), the greatest simulated increases in ET from the SWAT model occurred in high-elevation soils falling into the highest AWC bin (>91 mm) offering the most water capacity for plants (Fig. 9a and b). These simulations occurred in subbasins 9 and 22 of the upper elevation bin (sandy loam soils of the Notned series), and subbasins 1 and 2 of the mid-upper elevation bin (sandy loam soils of the Gerle series) (Fig. 1, Supplement Fig. S1). For these soils in the upper elevation bin (subbasins 9 and 22), over half of the simulations in the prediction uncertainty range of SWAT exceeded the STS prediction for the mildest warming case (Supplement Fig. S7a, substrate bin AWC-2). These "hot spots" of ET-change are localized, covering only 6% of these subbasins (Supplement Fig. S7d). Shifting from hot spots to "cold spots," the lowest simulated increases in ET from SWAT for the mildest warming case occurred in subbasins of the mid-lower elevation bin (Fig. 9a and b). This elevation range corresponds to the zone of minimum ET-increase shown in Fig. 6a. These modeled responses occurred in loamy sand (Toem series) of subbasin 20, and sandy loam (Shaver series) of subbasin 34 (Fig. 1, Supplement Fig. S1). With regard to watershed model uncertainty, exposed bedrock in the upper elevations of the watershed exhibited relatively low prediction uncertainties from SWAT (Fig. 9c).

5. Discussion

5.1. Choice of space-for-time substitution method

Our finding of substantial differences in high-elevation ET-sensitivity to temperature between a space-for-time substitution (STS) model and an integrated watershed model would remain unchanged if we had employed other STS methods (e.g., studies described in Supplement Section S1). For example, the watershed-scale ET-sensitivity to temperature from our STS model was 17 mm yr^{-1} $°C^{-1}$ over a 0–4 °C range of warming (Fig. 6a and b). The upper elevations contributed most (two-thirds) to the total volumetric changes in ET. In comparison, using an STS method based on nonlinear regression between ET, temperature, and precipitation, Goulden and Bales (2014) estimated an ET-sensitivity to temperature of approximately 30 mm yr^{-1} $°C^{-1}$ in the upper Kings River watershed neighboring to the south. Their prediction was attributed mainly to ET responses above 2000 m elevation (i.e., near the median elevation of our study area). Moreover, we showed in Supplement Section S1 that predicted long-term changes in runoff yield based on the STS method of Berghuijs et al. (2014) would be similar to values based on the above method of Goulden and Bales (2014). Therefore, the differences in ET-sensitivity to air temperature between our STS model and integrated watershed model would likely be greater if we had employed other previously used STS methods.

5.2. Factors behind ΔET differences between watershed model and STS model

We recognized three possible factors contributing to differences in predicted ET-sensitivity to air temperature between the STS and SWAT models. The first and perhaps most apparent factor is the strong elevational dependence of substrate AWC and ground slope in our study area, properties implicitly varied between scenarios of the STS model (and STS models in general) via translations in Budyko space (Fig. 2c) but not varied between scenarios of the SWAT model. The range in SWAT-modeled ET-sensitivities to temperature across the AWC bins at upper elevations, 16 mm yr^{-1} $°C^{-1}$ (box averages in Fig. 7a, left), exceeded the simulated value averaged across those same AWC bins, 9 mm yr^{-1} $°C^{-1}$ (short-dashed line Fig. 7a, left). This indicates that the spatial variability in substrate AWC is particularly important to consider in predictions of ET sensitivity to temperature at high elevations of this watershed. However, the influence of substrate properties appears to be temperature-dependent, as the differences in ET-sensitivity to temperature across different AWC bins in Fig. 7 become smaller with progressive warming. In the upper San Joaquin River watershed, high-elevation responses of ET to warming are strongly mediated by the abundance of exposed bedrock on steep slopes and the paucity of thick soils on gentle slopes (Fig. 7d). These characteristics can determine whether warming-induced increases in potential ET translate to increases or decreases in actual ET. In other watersheds exhibiting less variation in substrate AWC with elevation, substrate properties may play a lesser role in long-term ET responses to warming. The second possible factor is the tendency for a snow-to-rain transition to mute (offset) any increases in ET relative to the changes that would occur in the absence of such phase transition (Jeton and Dettinger, 1996; Risbey and Entekhabi, 1996; Dettinger et al., 2004; Tague et al., 2009). This effect would occur if the snow-to-rain transition causes the timing of water availability to become more out of sync from the seasonal timing of potential ET. This phenomenon is well illustrated in our SWAT model results by zones of minimum ET-increase that follow the rain-snow transition zone to higher elevations with progressive warming. These zones may correspond to the zones of maximum change in summer water deficit simulated for the upper Merced River watershed by Tague et al. (2009), which also migrated to higher elevations with progressive warming. In our simulations, mildest warming (2 °C) in the mid-lower elevation bin produced a relatively weak ET response (Fig. 7a) that was substantially below the STS prediction. We attribute this to

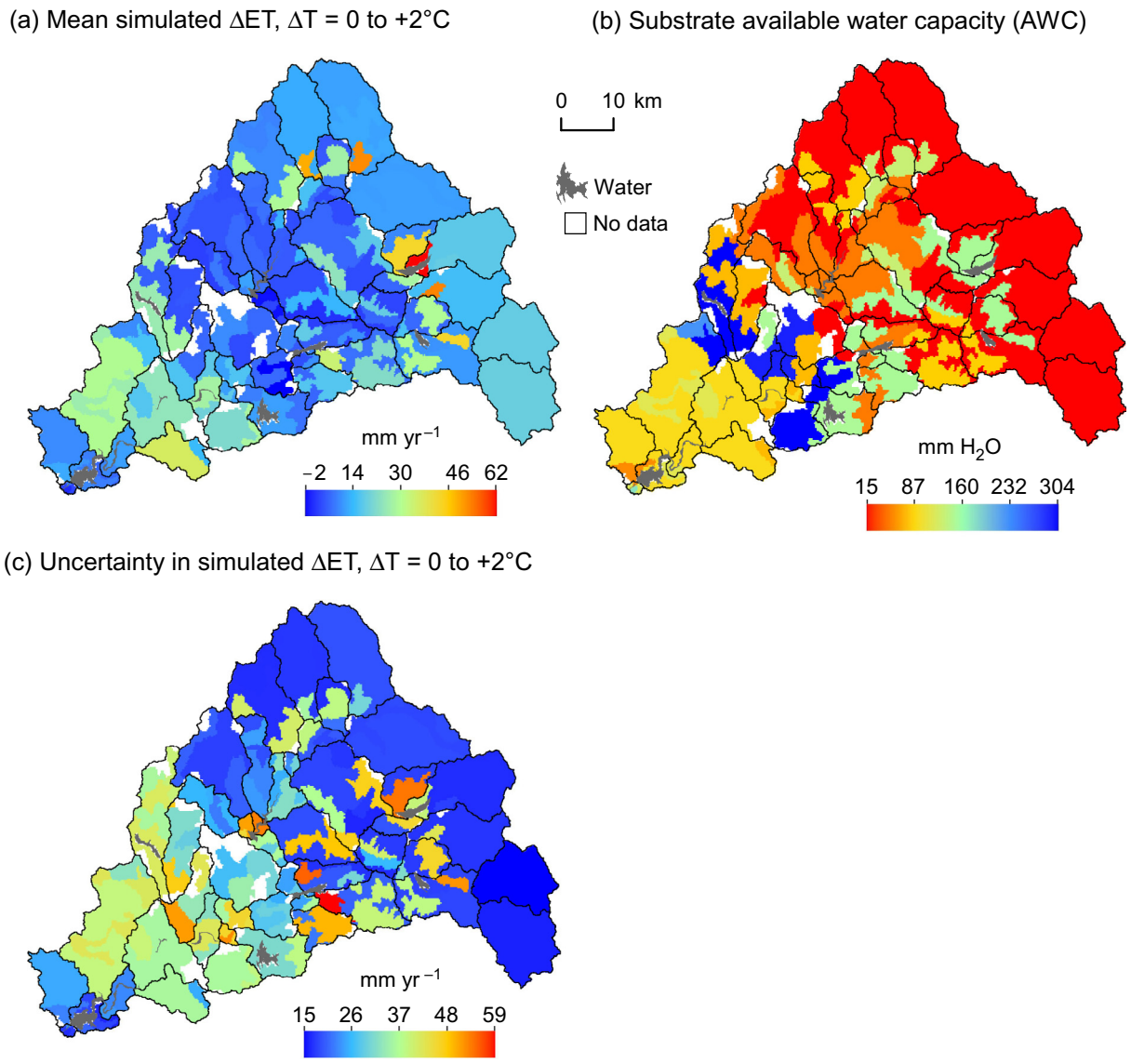
(a) Mean simulated ΔET, ΔT = 0 to +2°C
mm yr−1
−2 14 30 46 62
(b) Substrate available water capacity (AWC)
0 10 km
Water
No data
mm H2O
15 87 160 232 304
(c) Uncertainty in simulated ΔET, ΔT = 0 to +2°C
mm yr−1
15 26 37 48 59

Fig. 9. SWAT-modeled, long-term changes in ET for the substrate units in each subbasin of the watershed. Results shown for the 0–2 °C warming scenario. (a) Mean simulation in the 95% prediction uncertainty range, (b) substrate available water capacity (AWC), and (c) prediction uncertainty given as the difference between the maximum and minimum values in the prediction uncertainty ranges.

the above muting effect of a snow-to-rain transition. With further warming, ET responses in this elevation bin become stronger and more in line with the STS prediction (Fig. 7b and c), as this region becomes too warm to remain in the rain-snow transition zone. The third factor is the effect of warming on the distribution of forest species (Kelly and Goulden, 2008; Goulden et al., 2012), an effect that is implicitly included in STS models (including ours). We implicitly included this effect by assuming a temporal stationarity in the lapse-rate of potential ET versus elevation (Section 3.3). The effect of warming on forest properties represents a potentially important interaction between climate and potential ET, and was not simulated in our SWAT model which varied only air temperature while holding all other factors fixed.

5.3. Effect of landscape properties on high-elevation ET sensitivities to temperature

Our SWAT watershed model results suggest that high elevations of the upper San Joaquin River watershed will exhibit a large range in ET-sensitivities to air temperature owing to the coexistence of exposed bedrock interspersed with sparse soils, high topographic relief, and energy-limited conditions (Fig. 2c). Widespread areas of bedrock, covering approximately three-fourths of the upper watershed, exhibited muted (low) ET-responses to warming in terms of magnitudes and uncertainties (Figs. 7 and 9). This is attributed to limited infiltration and water holding capacities (Supplement Table S1), resulting in an abundance of rapid flow paths (i.e., overland and lateral flow) out of subbasins. Rapid flows are conducive to limited water availability during relatively warm conditions (Troch et al., 2013, Garcia and Tague, 2015), and may also cause snow-to-rain transitions to produce more asynchronous changes in timing of water availability and water demand (Tague et al., 2009) than would occur for substrates with greater infiltration and water holding capacities. Weathered bedrock is known to potentially be an important source of water for vegetation (Witty et al., 2003; Bales et al., 2011; Kitajima et al., 2013). Although this source of water was included in our SWAT model simulations (as "REVAP"), and was calibrated over the suggested range (Supplement Table S5, controlling parameter "GW_REVAP"), its influence was not sufficient to produce strong ET responses to warming in high-elevation areas lacking soils.

The relatively low values and uncertainties in simulated ET-responses to warming in high-elevation areas of exposed bedrock suggests with relative certainty that runoff yields from these areas will be resilient to warming. This may provide a useful insight for spatial assessments of future water supplies in high-elevation regions. Predictions of future runoff timing, needed for water management and planning, would benefit from the use of GCM-based climate projections (e.g., Miller et al., 2003; Dettinger et al., 2004; Ficklin et al., 2012).

The SWAT model produced particularly strong ET-responses to warming in high-elevation sandy loams (Notned and Gerle series) of the upper and mid-upper elevation bins of the watershed (Section 4.3, Figs. 1 and 9a). The greatest simulated ET-responses occurred in the Notned soil series of subbasin 9 (Fig. 1) for the mildest warming case (0–2 °C), with a mean simulation of + 69 mm yr^{-1} (+20% change) and a maximum simulation of +83 mm yr^{-1} (+20% change) in the 95% prediction uncertainty range (Supplement Fig. S7a and Table S11). Vegetation responses to warming in these localized "hot spots" of ET-change will likely contrast markedly with vegetation responses in neighboring areas where soils are thin or absent (Section 4.3; Figs. 7–9; Supplement Fig. S7), a finding that is consistent with observation-based studies demonstrating the important effect of soil and regolith properties on the composition and growth rate of forests (Witty et al., 2003; Meyer et al., 2007; Osborn et al., 2014).

Our findings also expand on the work of Tague et al. (2009) by clarifying the important role of hydrogeology and slope on warming-induced responses of ET in high-elevation, energy-limited regions. Using the RHESSys watershed model, Tague et al. (2009) showed that ET could increase by approximately 20% in response to 4 °C warming at high-elevations of the central Sierra Nevada. We showed that similar percent changes in long-term ET are possible at high-elevations of the upper San Joaquin River watershed (Fig. 7, Supplement Table S10), but that they would be limited to sparse areas containing relatively thick soils on gentle slopes.

High-elevation areas of exposed bedrock and sparse soils (e.g., Notned, Gerle series), which will likely exhibit contrasting responses of ET to warming, may provide interesting paired study sites for examining the role of hydrogeology on forest responses to potential climate change. High-elevation soils in the Notned and Gerle soil series can be located from the maps in Fig. 1 and Supplement Fig. S1, and the soil descriptions in Supplement Table S1. The Notned soil series consists of deep (exceeding 1.4 m), well-drained soils formed in colluvium or glacial material consisting of bouldery, coarse sandy loam (https://soilseries.sc.egov.usda.gov/). The Gerle soil series consists of deep (exceeding 1.5 m), well-drained soils formed in glacial till, glacial outwash, and alluvium consisting of sandy loam (https://soilseries.sc.egov.usda.gov/). We attribute the strong ET-responses of these soils at high elevations to a combination of low baseline aridity ratios (PET/P), indicative of energy-limitations (Fig. 2c), and abundant snowmelt to satisfy water demands during the growing season. Possible reasons for the apparent decreasing influence of soil types on ET-increases at progressively higher temperatures, noted in Section 4.3, are not entirely clear, but may include large-scale shifts from energy- to water-limitations as per the Budyko framework, and water-limitations associated with upward shifts of the rain-snow transition zone to higher elevations with progressive warming (Section 5.2).

6. Conclusion

Our objective in this study was to examine the spatial variability in long-term responses of ET to increased air temperature across different elevations, substrate available water capacities, and slopes of a snow-influenced watershed. We did this by comparing simulations from an integrated watershed model (SWAT) to those from a space-for-time substitution (STS) model that used the Budyko hypothesis in conjunction with long-term water flux observations. The greatest spatial variability in SWAT model results occurred for relatively mild warming (0–2 °C) of subbasins in the highest elevation bin examined, 2800–3420 m (upper quartile of watershed). Here, simulated increases in ET from SWAT ranged from 17 mm yr^{-1} (+7% change) in exposed bedrock on all slopes, to 69 mm yr^{-1} (+20% change) in sparsely distributed sandy loam soil on gentle slopes (<20% grade). The upper end of this range exceeded predictions from the STS model at these elevations, demonstrating that the watershed model could produce high-elevation ET responses at least as strong as the STS model. However, because of the preponderance of exposed bedrock and steep terrain at the higher elevations, the SWAT and STS models produced markedly different ET responses for both the upper elevation bin and watershed as a whole. The STS model produced watershed-scale increases in ET a factor of 2.3–2.6 greater than those from the SWAT model (depending on warming scenarios), with the upper half of the watershed contributing most (approximately two-thirds) to these differences. These results suggest that watershed-scale responses of ET to warming from integrated watershed models may be substantially lower, by a factor of 2–3 in our study, than predictions from space-for-time substitution models for snow-influenced, high-elevation systems such as the upper San Joaquin River watershed. Our results also suggest that long-term responses of vegetation water-use and stream runoff to warming in high-elevation, energy-limited regions will depend strongly on local hydrogeologic conditions, which can show great variability with elevation and exhibit physical evolution on a millennial timescale (Holbrook et al., 2014).

Acknowledgments

Technical assistance was provided by Karim Abbaspour, Otto Alvarez, Jacob Flanagan, Jon Herman, Xiande Meng, and Phil Saksa. Funding was provided by the U.S. National Science Foundation (NSF) Award # CBET-1204841 (Water Sustainability & Climate Program) and by the Inter-American Institute for Global Change Research (IAI) CRN3038 (under NSF Award # GEO-1128040). We thank two anonymous reviewers and the journal editorial team for their helpful comments that improved the manuscript.

Appendix A. Supplementary data

Supplementary data associated with this article can be found, in the online version, at https://doi.org/10.1016/j.jhydrol.2017.11.042.

References

Abbaspour, K.C., Johnson, C.A., van Genuchten, M.Th., 2004. Estimating uncertain flow and transport parameters using a sequential uncertainty fitting procedure. Vadose Zone J. 3, 1340–1352. https://doi.org/10.2136/vzj2004.1340.

Abbaspour, K.C., Yang, J., Maximov, I., Siber, R., Bogner, K., Mieleitner, J., Zobrist, J., Srinivasan, R., 2007. Modelling hydrology and water quality in the pre-alpine/alpine Thur watershed using SWAT. J. Hydrol. 333, 413–430. https://doi.org/10.1016/j.jhydrol.2006.09.014.

Ahl, R.S., Woods, S.W., Zuuring, H.R., 2008. Hydrologic calibration and validation of SWAT in a snow-dominated Rocky Mountain watershed, Montana, USA. J. Am. Water Resour. Assoc. 44, 1411–1430. https://doi.org/10.1111/j.1752-1688.2008.00233.x.

Arnold, J.G., Moriasi, D.N., Gassman, P.W., Abbaspour, K.C., White, M.J., Srinivasan, R., Santhi, C., Harmel, R.D., van Griensven, A., Van Liew, M.W., Kannan, N., Jha, M. K., 2012. SWAT: model use, calibration, and validation. Trans. ASABE 55, 1491–1508. https://doi.org/10.13031/2013.42256.

Bales, R.C., Hopmans, J.W., O'Geen, A.T., Meadows, M., Hartsough, P.C., Kirchner, P., Hunsaker, C.T., Beaudette, D., 2011. Soil moisture response to snowmelt and rainfall in a Sierra Nevada mixed-conifer forest. Vadose Zone J. 10, 786–799. https://doi.org/10.2136/vzj2011.0001.

Barnett, T.P., Adam, J.C., Lettenmeir, D.P., 2005. Potential impacts of a warming climate on water availability in snow-dominated regions. Nature 438, 303–309. https://doi.org/10.1038/nature04141.

Barnhart, T.B., Molotch, N.P., Livneh, B., Harpold, A.A., Knowles, J.F., Schneider, D., 2016. Snowmelt rate dictates streamflow. Geophys. Res. Lett. 43, 8006–8016. https://doi.org/10.1002/2016GL069690.

Berghuijs, W.R., Woods, R.A., Hrachowitz, M., 2014. A precipitation shift from snow towards rain leads to a decrease in streamflow. Nat. Clim. Change 4, 583–586. https://doi.org/10.1038/nclimate2246.

Budyko, M.I., 1974. Climate and Life. Academic Press, New York (accessed from EBSCOhost on 11.05.17, unr.idm.oclc.org/login?url=http://search.ebscohost.com/login.aspx?direct=true&db=e025xna&AN=297011&site=ehost-live&scope=site).

Cayan, D.R., Maurer, E.P., Dettinger, M.D., Tyree, M., Hayhoe, K., 2008. Climate change scenarios for the California region. Clim. Change 87 (Suppl. 1), S21–S42. https://doi.org/10.1007/s10584-007-9377-6.

Clow, D.W., 2010. Changes in the timing of snowmelt and streamflow in Colorado: a response to recent warming. J. Clim. 23, 2293–2306. https://doi.org/10.1175/2009JCLI2951.1.

Costa-Cabral, M., Roy, S.B., Maurer, E.P., Mills, W.B., Chen, L., 2013. Snowpack and runoff response to climate change in Owens Valley and Mono Lake watersheds. Clim. Change 116, 97–109. https://doi.org/10.1007/s10584-012-0529-y.

Dai, A., 2008. Temperature and pressure dependence of the rain-snow phase transition over land and ocean. Geophys. Res. Lett. 35, L12802. https://doi.org/10.1029/2008GL033295.

Dettinger, M.D., Cayan, D.R., Meyer, M.K., Jeton, A.E., 2004. Simulated hydrologic responses to climate variations and change in the Merced, Carson, and American River basins, Sierra Nevada, California, 1900–2099. Clim. Change 62, 283–317. https://doi.org/10.1023/B:CLIM.0000013683.13346.4f.

Duell, L.F.W., 1994. The sensitivity of northern Sierra Nevada streamflow to climate change. J. Am. Water Resour. Assoc. 30, 841–859. https://doi.org/10.1111/j.1752-1688.1994.tb03333.x.

Ficklin, D.L., Stewart, I.T., Maurer, E.P., 2012. Projections of 21st century Sierra Nevada local hydrologic flow components using an ensemble of general circulation models. J. Am. Water Resour. Assoc. 48, 1104–1125. https://doi.org/10.1111/j.1752-1688.2012.00675.x.

Fontaine, T.A., Cruickshank, T.S., Arnold, J.G., Hotchkiss, R.H., 2002. Development of a snowfall-snowmelt routine for mountainous terrain for the soil water assessment tool (SWAT). J. Hydrol. 262, 209–223. https://doi.org/10.1016/S0022-1694(02)00029-X.

Garcia, E.S., Tague, C.L., 2015. Subsurface storage capacity influences climate–evapotranspiration interactions in three western United States catchments. Hydrol. Earth Syst. Sci. 19, 4845–4858. https://doi.org/10.5194/hess-19-4845-2015.

Giger, D.R., Schmitt, G.J., 1993. Soil Survey of Sierra National Forest Area, California. United States Department of Agriculture, Forest Service, Pacific Southwest Region, 150 p. (plus maps) (accessed on 17.11.16 at https://www.nrcs.usda.gov/Internet/FSE_MANUSCRIPTS/california/sierraNFCA1983/).

Godsey, S.E., Kirchner, J.W., Tague, C.L., 2014. Effects of changes in winter snowpacks on summer low flows: case studies in the Sierra Nevada, California, USA. Hydrol. Process. 28, 5048–5064. https://doi.org/10.1002/hyp.9943.

Goulden, M.L., Anderson, R.G., Bales, R.C., Kelly, A.E., Meadows, M., Wilson, G.C., 2012. Evapotranspiration along an elevation gradient in California's Sierra Nevada. J. Geophys. Res. 117, G03028. https://doi.org/10.1029/2012JG002027.

Goulden, M.L., Bales, R.C., 2014. Mountain runoff vulnerability to increased evapotranspiration with vegetation expansion. Proc. Natl. Acad. Sci. U. S. A. 111, 14071–14075. https://doi.org/10.1073/pnas.1319316111.

Grusson, Y., Sun, X., Gascoin, S., Sauvage, S., Raghavan, S., Anctil, F., Sáchez-Pérez, J.-M., 2015. Assessing the capability of the SWAT model to simulate snow, snow melt and streamflow dynamics over an alpine watershed. J. Hydrol. 531, 574–588. https://doi.org/10.1016/j.jhydrol.2015.10.070.

Guan, B., Molotch, N.P., Waliser, D.E., Jepsen, S.M., Painter, T.H., Dozier, J., 2013. Snow water equivalent in the Sierra Nevada: blending snow sensor observations with snowmelt model simulations. Water Resour. Res. 49, 5029–5046. https://doi.org/10.1002/wrcr.20387.

Harpold, A., Brooks, P., Rajagopal, S., Heidbuchel, I., Jardine, A., Stielstra, C., 2012. Changes in snowpack accumulation and ablation in the intermountain west. Water Resour. Res. 48, W11501. https://doi.org/10.1029/2012WR011949.

He, Z., Wang, Z., Suen, C.J., Ma, X., 2013. Hydrologic sensitivity of the upper San Joaquin River watershed in California to climate change scenarios. Hydrol. Res. 44, 723–736. https://doi.org/10.2166/nh.2012.441.

Herman, J., Usher, W., 2017. SALib: an open-source Python library for sensitivity analysis (software accessed on 08.12.16 at) J. Open Source Softw. 2 (9), 1–2. https://doi.org/10.21105/joss.00097.

Holbrook, W.S., Riebe, C.S., Elwaseif, M., Hayes, J.L., Basler-Reeder, K., Harry, D.L., Malazian, A., Dosseto, A., Hartsough, P.C., Hopmans, J.W., 2014. Geophysical constraints on deep weathering and water storage potential in the Southern Sierra Critical Zone Observatory. Earth Surf. Process. Landforms 39, 366–380. https://doi.org/10.1002/esp.3502.

Hunsaker, C.T., Whitaker, T.W., Bales, R.C., 2012. Snowmelt runoff and water yield along elevation and temperature gradients in California's southern Sierra Nevada. J. Am. Water Resour. Assoc. 48 (4), 667–678. https://doi.org/10.1111/j.1752-1688.2012.00641.x.

IPCC, 2014. Climate Change 2014: Synthesis Report. Contribution of Working Groups I, II and III to the Fifth Assessment Report of the Intergovernmental Panel on Climate Change. In: Core Writing Team, Pachauri, R.K., Meyer, L.A. (Eds.), IPCC, Geneva, Switzerland, 151 pp. (accessed on 28.11.16 at https://www.ipcc.ch/report/ar5/syr/).

Jepsen, S.M., Harmon, T.C., Hunsaker, C.T., Meadows, M.W., 2016. Hydrogeologic influence on changes in snowmelt runoff with climate warming: numerical experiments on a mid-elevation catchment in the Sierra Nevada, USA. J. Hydrol. 533, 332–342. https://doi.org/10.1016/j.jhydrol.2015.12.010.

Jeton, A.E., Dettinger, M.D., Smith, J.L., 1996. Potential effects of climate change on streamflow, eastern and western slopes of the Sierra Nevada, California and Nevada. Water-Resources Investigations Report 95-4260, U.S. Geological Survey, 44 p.

Kelly, A.E., Goulden, M.L., 2008. Rapid shifts in plant distribution with recent climate change. Proc. Natl. Acad. Sci. U. S. A. 105, 11823–11826. https://doi.org/10.1073/pnas.0802891105.

Kitajima, K., Allen, M.F., Goulden, M.L., 2013. Contribution of hydraulically lifted deep moisture to the water budget in a Southern California mixed forest. J. Geophys. Res. Biogeosci. 118, 1561–1572. https://doi.org/10.1002/2012JG002255.

Klos, P.Z., Link, T.E., Abatzoglou, J.T., 2014. Extent of the rain-snow transition zone in the western U.S. under historic and projected climate. Geophys. Res. Lett. 14, 4560–4568. https://doi.org/10.1002/2014GL060500.

Lenderink, G., van Meijgaard, E., 2008. Increase in hourly precipitation extremes beyond expectations from temperature changes. Nat. Geosci. 1, 511–514. https://doi.org/10.1038/ngeo262.

Luce, C.H., Abatzoglou, J.T., Holden, Z.A., 2013. The missing mountain water: slower westerlies decrease orographic enhancement in the Pacific Northwest USA. Science 342, 1360–1364. https://doi.org/10.1126/science.1242335.

Lundquist, J.D., Loheide, S.P., 2011. How evaporative water losses vary between wet and dry water years as a function of elevation in the Sierra Nevada, California, and critical factors for modeling. Water Resour. Res. 47, W00H09. https://doi.org/10.1029/2010WR010050.

MAH, 2003. Upper San Joaquin River Basin Storage Investigation: Phase 1 Investigation Report. A Joint Study by Bureau of Reclamation Mid-Pacific Region and California Department of Water Resources in Coordination with the California Bay-Delta Authority, Report Prepared by MAH, 128 pp. (accessed 25.01.17 from https://www.usbr.gov/mp/sccao/storage/docs/phase1_rpt_fnl/12_complete_rpt.pdf).

Maurer, E.P., Wood, A.W., Adam, J.C., Lettenmaier, D.P., Nijssen, B., 2002. A long-term hydrologically-based data set of land surface fluxes and states for the conterminous United States. J. Clim. 15, 3237–3251. https://doi.org/10.1175/1520-0442(2002)015<3237:ALTHBD>2.0.CO;2.

McVicar, T.R., Van Niel, T.G., Li, L.T., Hutchinson, M.F., Mu, X.M., Liu, Z.H., 2007. Spatially distributing monthly reference evapotranspiration and pan evaporation considering topographic influences. J. Hydrol. 338, 196–220. https://doi.org/10.1016/j.jhydrol.2007.02.018.

McVicar, T.R., Van Niel, T.G., Roderick, M.L., Li, L.T., Mo, X.G., Zimmermann, N.E., Schmatz, D.R., 2010. Observational evidence from two mountainous regions that near-surface wind speeds are declining more rapidly at higher elevations than lower elevations: 1960–2006. Geophys. Res. Lett. 37, L06402. https://doi.org/10.1029/2009GL042255.

McVicar, T.R., Roderick, M.L., Donohue, R.J., Li, L.T., Van Niel, T.G., Thomas, A., Grieser, J., Jhajharia, D., Himri, Y., Mahowald, N.M., Mescherskaya, A.V., Kruger, A.C., Rehman, S., Dinpashoh, Y., 2012. Global review and synthesis of trends in observed terrestrial near-surface wind speeds: implications for evaporation. J. Hydrol. 416–417, 182–205. https://doi.org/10.1016/j.jhydrol.2011.10.024.

Merz, R., Blöschl, G., 2009. A regional analysis of event runoff coefficients with respect to climate and catchment characteristics in Austria. Water Resour. Res. 45, W01405. https://doi.org/10.1029/2008WR007163.

Meyer, M.D., North, M.P., Gray, A.N., Zald, H.S.J., 2007. Influence of soil thickness on stand characteristics in a Sierra Nevada mixed-conifer forest. Plant Soil 294, 113–123. https://doi.org/10.1007/s11104-007-9235-3.

Miller, N.L., Bashford, K.E., Strem, E., 2003. Potential impacts of climate change on California Hydrology. J. Am. Water Resour. Assoc. 39, 771–784. https://doi.org/10.1111/j.1752-1688.2003.tb04404.x.

Milly, P.C.D., 1994. Climate, soil water storage, and the average annual water balance. Water Resour. Res. 30, 2143–2156. https://doi.org/10.1029/94WR00586.

Milly, P.C.D., Dunne, K.A., 2011. On the hydrologic adjustment of climate-model projections: the potential pitfall of potential evapotranspiration. Earth Interact. 15, 1–14. https://doi.org/10.1175/2010EI363.1.

Milley, P.C.D., Dunne, K.A., 2016. Potential evapotranspiration and continental drying. Nat. Clim. Change 6, 946–949. https://doi.org/10.1038/nclimate3046.

Nash, J.E., Sutcliffe, J.V., 1970. River flow forecasting through conceptual models: Part 1. A discussion of principles. J. Hydrol. 10, 282–290. https://doi.org/10.1016/0022-1694(70)90255-6.

Neitsch, S.L., Arnold, J.G., Kiniry, J.R., Srinivasan, R., Williams, J.R., 2002. Soil and Water Assessment Tool User's Manual Version 2000. Texas Water Resources Institute, College Station, Texas, 413 pp. (accessed 13.03.15 at http://swat.tamu.edu/documentation/).

Neitsch, S.L., Arnold, J.G., Kiniry, J.R., Williams, J.R., 2011. Soil and Water Assessment Tool Theoretical Documentation Version 2009. Texas Water Resources Institute

Technical Report No. 406, College Station, Texas, 618 pp. (accessed 13.03.15 at http://swat.tamu.edu/documentation/).
Null, S.E., Viers, J.H., Mount, J.F., 2010. Hydrologic response and watershed sensitivity to climate warming in California's Sierra Nevada. PLoS ONE 5, e9932. https://doi.org/10.1371/journal.pone.0009932.
B. Osborn, W. Chapple, B. Ewers, D. Williams, Sensitivity of photosynthetic gas exchange and growth of Lodgepole Pine to climate variability depends on the age of Pleistocene glacial surfaces, in: Abstract H31G-0704 (Poster) Presented at 2014 Fall Meeting, AGU, 15–19 December, San Francisco, California, 2014.
Pandey, G.R., Cayan, D.R., Georgakakos, K.P., 1999. Precipitation structure in the Sierra Nevada of California during winter. J. Geophys. Res. Atmos. 104 (D10), 12019–12030. https://doi.org/10.1029/1999JD900103.
Peters, N.E., Aulenbach, B.T., 2011. Water storage at the Panola Mountain Research Watershed, Georgia, USA. Hydrol. Process. 25, 3878–3889. https://doi.org/10.1002/hyp.8334.
Pierce, D.W., Cayan, D.R., Das, T., Maurer, E.P., Miller, N.L., Bao, Y., Kanamitsu, M., Yoshimura, K., Snyder, M.A., Sloan, L.C., Franco, G., Tyree, M., 2013. The key role of heavy precipitation events in climate model disagreements of future annual precipitation changes in California. J. Clim. 26, 5879–5896. https://doi.org/10.1175/JCLI-D-12-00766.1.
Potter, C., 2015. Vegetation cover change in the Upper Kings River basin of the Sierra Nevada detected using Landsat satellite image analysis. Clim. Change 131, 635–647. https://doi.org/10.1007/s10584-015-1397-z.
Reinfelds, I., Swanson, E., Cohen, T., Larsen, J., Nolan, A., 2014. Hydrospatial assessment of streamflow yields and effects of climate change: Snowy Mountains, Australia. J. Hydrol. 512, 206–220. https://doi.org/10.1016/j.jhydrol.2014.02.038.
Risbey, J.S., Entekhabi, D., 1996. Observed Sacramento Basin streamflow response to precipitation and temperature changes and its relevance to climate impact studies. J. Hydrol. 184, 209–223. https://doi.org/10.1016/0022-1694(95)02984-2.
Safeeq, M., Shukla, S., Arismendi, I., Grant, G.E., Lewis, S.L., Nolin, A., 2016. Influence of winter season climate variability on snow–precipitation ratio in the western United States. Int. J. Climatol. 36, 3175–3190. https://doi.org/10.1002/joc.4545.
Saltelli, A., Ratto, M., Andres, T., Campolongo, F., Cariboni, J., Gatelli, D., Saisana, M., Tarantola, S., 2008. Global Sensitivity Analysis: The Primer. John Wiley & Sons Ltd, Chichester, England, 306 pp. (accessed 08.12.16 at http://www.eblib.com).
Santhi, C., Arnold, J.G., Williams, J.R., Dugas, W.A., Srinivasan, R., Hauck, L.M., 2001. Validation of the SWAT model on a large river basin with point and nonpoint sources. J. Am. Water Resour. Assoc. 37, 1169–1188. https://doi.org/10.1111/j.1752-1688.2001.tb03630.x.
Seager, R., Ting, M., Li, C., Naik, N., Cook, B., Nakamura, J., Liu, H., 2013. Projections of declining surface-water availability for the southwestern United States. Nat. Clim. Change 3, 482–486. https://doi.org/10.1038/nclimate1787.
Stewart, I.T., Cayan, D.R., Dettinger, M.D., 2005. Changes toward earlier streamflow timing across western North America. J. Clim. 18, 1136–1155. https://doi.org/10.1175/JCLI3321.1.
Tague, C., Heyn, K., Christensen, L., 2009. Topographic controls on spatial patterns of conifer transpiration and net primary productivity under climate warming in mountain ecosystems. Ecohydrology 2, 541–554. https://doi.org/10.1002/eco.88.
Tague, C., Peng, H., 2013. The sensitivity of forest water use to the timing of precipitation and snowmelt recharge in the California Sierra: implications for a warming climate. J. Geophys. Res. Biogeosci. 118, 875–887. https://doi.org/10.1002/jgrg.20073.
Trancoso, R., Larsen, J.R., McVicar, T.R., Phinn, S.R., McAlpine, C.A., 2017. CO_2-vegetation feedbacks and other climate changes implicated in reducing base flow. Geophys. Res. Lett. 44, 2310–2318. https://doi.org/10.1002/2017GL072759.
Troch, P.A., Carrillo, G., Sivapalan, M., Wagener, T., Sawicz, K., 2013. Climate-vegetation-soil interactions and long-term hydrologic partitioning: signatures of catchment co-evolution. Hydrol. Earth Syst. Sci. 17, 2209–2217. https://doi.org/10.5194/hess-17-2209-2013.
USDA, 1994. State Soil Geographic (STATSGO) Data Base: Data Use Information. U.S. Department of Agriculture, Natural Resources Conservation Service, Miscellaneous Publication Number 1492, 113 pp. (accessed 16.12.16 at http://www.fsl.orst.edu/pnwerc/wrb/metadata/soils/statsgo.pdf).
USGS, 2013. National Elevation Dataset (NED) 1 arc-second 2013 1×1 degree ArcGrid. U.S. Geological Survey, Reston, VA (accessed 11.12.14 at https://nationalmap.gov/).
USGS, 2014a. NLCD 2001 Land Cover (2011 Edition, Amended 2014) – National Geospatial Data Asset (NGDA) Land Use Land Cover. U.S. Geological Survey, Sioux Falls, SD (accessed 16.04.15 at http://www.mrlc.gov/nlcd01_data.php).
USGS, 2014b. National Hydrography Dataset (NHD) Medium Resolution for California 20140718 State or Territory Shapefile. U.S. Geological Survey, Reston, VA, (accessed 19.02.16 at https://nationalmap.gov/).
Van Liew, M.W., Arnold, J.G., Bosch, D.D., 2005. Problems and potential of autocalibrating a hydrologic model. Trans. ASAE 48, 1025–1040. https://doi.org/10.13031/2013.18514.
Vicuna, S., Dracup, J.A., 2007. The evolution of climate change impact studies on hydrology and water resources in California. Clim. Change 82, 327–350. https://doi.org/10.1007/s10584-006-9207-2.
Watson, B.M., Putz, G., 2014. Comparison of temperature-index snowmelt models for use within an operational water quality model. J. Environ. Qual. 43, 199–207. https://doi.org/10.2134/jeq2011.0369.
Westra, S., Alexander, L.V., Zwiers, F.W., 2013. Global increasing trends in annual maximum daily precipitation. J. Clim. 26, 3904–3918. https://doi.org/10.1175/JCLI-D-12-00502.1.
Westra, S., Fowler, H.J., Evans, J.P., Alexander, L.V., Berg, P., Johnson, F., Kendon, E.J., Lenderink, G., Roberts, N.M., 2014. Future changes to the intensity and frequency of short-duration extreme rainfall. Rev. Geophys. 52, 522–555. https://doi.org/10.1002/2014RG000464.
Wild, M., 2009. Global dimming and brightening: a review. J. Geophys. Res. 114, D00D16. https://doi.org/10.1029/2008JD011470.
Winchell, M., Srinivasan, R., Di Luzio, M., Arnold, J., 2013. ArcSWAT Interface for SWAT2012: User's Guide. U.S. Department of Agriculture Research Service; Grassland Soil and Water Research Laboratory, Temple, Texas, p. 459.
Witty, J.H., Graham, R.C., Hubbert, K.R., Doolittle, J.A., Wald, J.A., 2003. Contributions of water supply from the weathered bedrock zone to forest soil quality. Geoderma 114, 389–400. https://doi.org/10.1016/S0016-7061(03)00051-X.
Yang, J., Reichert, P., Abbaspour, K.C., Xia, J., Yang, H., 2008. Comparing uncertainty analysis techniques for a SWAT application to the Chaohe Basin in China. J. Hydrol. 358, 123. https://doi.org/10.1016/j.jhydrol.2008.05.012.
Zhang, X., Srinivasan, R., Debele, B., Hao, F., 2008. Runoff simulation of the headwaters of the Yellow River using the SWAT model with three snowmelt algorithms. J. Am. Water Resour. Assoc. 44, 48–61. https://doi.org/10.1111/j.1752-1688.2007.00137.x.
Zhou, S., Yu, B., Huang, Y., Wang, G., 2015. The complementary relationship and generation of the Budyko functions. Geophys. Res. Lett. 42, 1781–1790. https://doi.org/10.1002/2015GL063511.